Summary Report for Transition Intensity Calculation of Lanthanide-doped Nanocrystal $NaYF_4$ with Judd-Ofelt Theory

Chuanyu Liu*

March 26, 2024

Contents

1 Background **2**

2 Introduction **3**

3 Theoretical Review **4**
3.1 Electronic Structure of Trivalent Lanthanides Ln^{3+} . . . 4
3.1.1 Electrostatic Interaction(Coulomb Repulsion): $\widehat{H}_e$ . . . 4
3.1.2 Spin–Orbit Interaction: $\widehat{H}_{so}$ . . . 5
3.1.3 Free Ion Approximation . . . 5
3.2 Angular Momentum Coupling of Multi-electron Atoms . . . 6
3.2.1 Wigner Symbol . . . 6
3.2.2 Wigner–Eckart Theorem & Reduced Matrix Elements(RME) . . . 7
3.3 RME of Tensor Operators: $\widehat{U}^{(k)}$, $\widehat{V}^{(1x)}$, $\widehat{L}+g\widehat{S}$ . . . 7
3.3.1 $\widehat{U}^{(k)}$: Electric-dipole Transition Intensities . . . 8
3.3.2 $\widehat{V}^{(1x)}$: RME of Spin-Orbit Interaction Operator $\widehat{H}_{so}$ . . . 8
3.3.3 $\widehat{L}+g\widehat{S}$: Magnetic-dipole Transition Intensity . . . 9
3.4 Intermediate Coupling Scheme and Eigenvalues . . . 9
3.4.1 RME of Electrostatic Operator $\widehat{H}_e$ . . . 9
3.4.2 RME of Spin-Orbital Interaction Operator $\widehat{H}_{so}$ . . . 10
3.4.3 Eigenvalue equation $\widehat{H}=\widehat{H}_e+\widehat{H}_{so}$ . . . 11

4 Transitions Intensity of Lanthanide in Solids **12**
4.1 Transitions of 4f Electronic Configurations . . . 12
4.2 ED Oscillator Strengths . . . 14
4.3 MD Oscillator Strengths . . . 15
4.4 χ_{ED}^{abs}: Local Field Correction . . . 15
4.5 Refractive Index Dispersion of Materials(Sellmeier Equation) . . . 15

5 Derived Quantities **16**
5.1 Electric-dipole Transition . . . 16
5.1.1 Comparison with Emory's Model . . . 16
5.1.2 Comparison with Weber's Model . . . 17
5.1.3 Comparison with Takash's Model . . . 17
5.2 Magnetic-dipole Transition . . . 18
5.2.1 Comparison with Emory's Model . . . 18
5.2.2 Comparison with Weber's Model . . . 19
5.2.3 Comparison with Norman's Model . . . 20
5.3 Lifetime of Excited States . . . 20
5.4 Branch Ratios . . . 21
5.5 Multi-phonon Relaxation process(MPR) . . . 21

*Email: liuchuan@broadinstitute.org

6 Case study: $Yb^{3+}, Tm^{3+}, Er^{3+}$ in $NaYF_4$ **21**
6.1 Pure Wavefunction Approximation . . . 22
6.2 Basic Constants . . . 22
6.2.1 Judd-Ofelt Intensity Parameters Ω_λ . . . 22
6.2.2 Refractive Index n . . . 22
6.2.3 Local Field Correction χ . . . 23
6.3 Radiative Emission Intensity Calculation . . . 23
6.3.1 ED Radiative Rmission [Colab] . . . 23
6.3.2 MD Radiative Emission [Colab] . . . 23
6.4 Non-radiative Emission Intensity Calculation . . . 23
6.4.1 Multi-phonon Relaxation(MPR) [Colab] . . . 23
6.4.2 Phonon-assisted Energy Transfer(PET) [Colab] . . . 24
6.4.3 ET Energy Matching Condition . . . 25
6.5 Monte Carlo Simulation [Colab] . . . 27
6.5.1 Model Outputs . . . 27
6.6 Conclusion . . . 29
6.6.1 What I Have Achieved . . . 29
6.6.2 Simulation Results . . . 29

7 Summary & Outlook **29**
7.1 Model Evaluation . . . 29
7.1.1 Advantages . . . 29
7.1.2 Defects . . . 30
7.2 Potential Improvements . . . 30

8 Supplementary Information **31**
8.1 Reproduction of Others Parameters . . . 31
8.1.1 Emory, JPC, 2012 [Colab] . . . 31
8.1.2 Weber, Physical Review, 1967 [Colab] . . . 31
8.2 Experiments Fitting of Barycenter Energy E_B . . . 31
8.3 Experimental Fitting for Oscillator Strengths f . . . 32

9 Tables **33**
9.1 Calculated ED Transition Rates of Tm^{3+} . . . 33
9.2 Calculated ED Transition Rates of Er^{3+} . . . 35
9.3 Calculated MD Transition Rates of Tm^{3+} . . . 35
9.4 Calculated MD Transition Rates of Er^{3+} . . . 35
9.5 Calculated MPR Rates of Tm^{3+} . . . 35
9.6 Calculated MPR Rates of Er^{3+} . . . 35
9.7 Calculated Resonant ET Rates of Yb^{3+} . . . 35
9.8 Calculated Up-conversion Rates of Yb^{3+}-Tm^{3+} . . . 35
9.9 Calculated Cross-relaxation Rates of Tm^{3+}-Tm^{3+} . . . 35
9.10 Calculated Up-conversion Rates of Yb^{3+}-Er^{3+} . . . 35
9.11 Calculated Cross-relaxation Rates of Er^{3+}-Er^{3+} . . . 35
9.12 Emory: ED Transition Rates of Er^{3+}+Tm^{3+} . . . 35
9.13 Emory: ED Transition Rates of Er^{3+} . . . 35
9.14 Weber: ED Transition Rates of Er^{3+} . . . 35
9.15 Weber: MD Transition Rates of Er^{3+} ($n = 2.02$) . . . 35
9.16 Weber: MD Transition Rates of Er^{3+} ($n = 1.5$) . . . 35

1 Background

The theory on the 4f $\leftrightarrow$ 4f transition intensities introduced by B.R. Judd and G.S. Ofelt in 1962 has become a centerpiece in rare-earth optical spectroscopy over the past six decades. Two separate papers authored by Brian Judd(UC Berkeley) and George Ofelt(Johns Hopkins University), of which

over the years have become the origin of the Judd-Ofelt (J-O) Theory, were published independently in 1962, in Physical Review[1] and Journal of Chemical Physics[2], respectively.

The J-O theory is used widely for the theoretical description of the spectroscopic properties of the lanthanide-doped solid state materials. In fact it is the golden (and the only one) theoretical tool of f-electron spectroscopy, that is applied in ab initio type calculations[3]. It is indeed a unique tool applicable for all of these investigations whose main aim is to understand the physical mechanisms responsible for a plenty of properties observed for lanthanide materials.

Based on the literature I have read so far and to the best of my understanding, I will firstly present a general theoretical formalism of 4f electronic states and intermediate coupling wavefunctions, followed by simplified way to the calculation of 4f $\leftrightarrow$ 4f transition intensity with operator techniques in atomic spectroscopy developed by Judd, and finally implement our calculated parameters with Monte Carl simulation to reproduce experimental observation. My goal is to provide a reliable self-consistent model for experimental work, while a rigorous derivation of the mathematical foundations of the Judd–Ofelt theory and a comprehensive survey of its applications to lanthanide-doped nanomaterials is beyond the scope of the report. Some basic implications, limitations, and pitfalls of the theory are skipped temporarily, and some necessary simplifications are made in order to properly apply the theory to practical problems, but an extensive bibliography is attached as a guide map for future investigation. A case study integrated with Monte Carlo simulation is presented to show the model's performance of our recently published paper.

2 Introduction

The great appeal of the J–O theory is in its ability to predict electric-dipole(ED) oscillator strengths f_{ED}^{emi} in absorption/emission luminescence, branching ratios, excited-state radiative lifetimes, energy-transfer probabilities, and estimates of quantum efficiencies by using only three parameters: Ω_λ:

$$f_{ED}^{emi} = \frac{8\pi^2 m_e}{3h} \frac{v}{(2J+1)} n \chi_{ED}^{abs} S_{f\leftarrow i} \tag{1}$$

where:

- m_e (g): Electron mass
- h ($\mathrm{g \cdot cm^2 \cdot s^{-1}}$): Planck constant
- J: Total angular momentum quantum number of initial level
- ν ($\mathrm{s^{-1}}$): Mean transition frequency
- n: Refractive index at the transition frequency
- χ_{ED}^{abs}: Local field correction
- $S_{f\leftarrow i}$: Line strength

Among the Eq.(1), the most significant part is the line strength $S_{f\leftarrow i}$, and it is a common opinion that the task of reproduction of spectra of rare earth doped materials is reduced to the problem of adjusting at most three intensity parameters Ω_λ, which are known for **Judd-Ofelt intensity parameters**, in line strength $S_{f\leftarrow i}$ with the following expression, which is an algebraic scheme of the parametrization of the spectrum:

$$S_{f\leftarrow i} = \sum_{\lambda=2,4,6} \Omega_\lambda \left| \left\langle \Psi_f || U^{(\lambda)} || \Psi_i \right\rangle \right|^2 \tag{2}$$

the summation is over the even-rank reduced matrix elements $\lambda = 2, 4, 6$ of the $\widehat{U}^{(\lambda)}$ tensor operator. More details would be given in the following section 3.3.1.

3 Theoretical Review

3.1 Electronic Structure of Trivalent Lanthanides Ln^{3+}

The 3+ oxidation states Ln^{3+} are by far the most common for rare-earth ions in condensed matter. The 4f electrons are shielded quite effectively from the effects of the surrounding charges in a solid. This is a unique feature of the rare-earth ions. As one of its consequences, the wavefunctions and associated energy are rather insensitive to the chemical surroundings of the Ln^{3+} ion. Therefore, some approximation of ignoring the impact from surrounding environment is the fact that the coordinating environment has only a small influence on the well-shielded 4f electrons.

Although, 4f electrons have well-shielded properties, but the weak interactions of the Ln^{3+} with its surroundings affect both the effective electrostatic $\widehat{H}_e$ and spin–orbit coupling strength $\widehat{H}_{so}$ to some extent. As a result, more accurate calculation requires consideration of small crystal-field splittings($\widehat{H}_{CF}$) for Ln^{3+} ions in different solids. Although $\widehat{H}_{CF}$ only accounts for 20% compared with dominent interactions $\widehat{H}_e$ and $\widehat{H}_{so}$ in UCNPs, but it impacts the energy levels E_i in real system, that has significant effect in the construction of high-quality intermediate coupling wavefunctions as required by Judd-Ofelt theory. More details about experimental fitting of E_i are given in Support Information 8.2.

The electron configuration of Ln^{3+} is $[Xe]4f^N$, where N runs from 1 $\left(Ce^{3+}\right)$ to 13 $\left(Yb^{3+}\right)$ along the series of Ln^{3+} ions. The 4f-orbitals are empty for $La^{3+}(N = 0)$ and filled fully for $Lu^{3+}(N = 14)$, and these ions therefore do not have any 4f $\leftrightarrow$ 4f transitions. In this report, we only discuss three types of ions: Er^{3+}, Tm^{3+}, and Yb^{3+}, which are $[Xe]4f^{11}$, $[Xe]4f^{12}$, and $[Xe]4f^{13}$, respectively.

3.1.1 Electrostatic Interaction(Coulomb Repulsion): $\widehat{H}_e$

As a result of the electrostatic interaction(Coulomb repulsion), for multi-electron atom, we can consider in 4f subshell there are N electrons spins s_i and the N electrons orbital angular momentum l_i to combine separately to form a total spin angular momentum $S = \sum s_i$ with a quantum number $M_S = -S, \ldots, S$ and total orbital angular momentum $L = \sum l_i$ with a quantum number $M_L = -L, \ldots, L$, respectively. There are also two constraints must be met:

- Pauli's Exclusion Principle. No two electrons in the same atom can have identical values for all four quantum numbers: s, m_l, l, n
- Hund's Rule. (1) The terms with the largest S values have the lowest energy values among all the terms of an electronic configuration. Among these terms, those with the highest L values have the lowest energy values. (2) For the terms in configuration with a number of electrons equal or exceeding that of the half-filled shell, the larger the J value, the lower the energy. On the other hand, if the number of electrons lower than that of half-filled shell, then the smaller the J values, the lower the energy. Namely, for the less-than-half filled 4f electron configurations, the energies of the J states within the same $^{2S+1}L_J$ manifold increase with increasing J, whereas the trend is inverted for the more-than-half filled configurations. For example, for the Pr^{3+} ion ($4f^2$) the ^3H_J ($J = 4, 5, 6$) levels in order of increasing energy are $^3H_4, ^3H_5, ^3H_6$. For the conjugate $4f^{12}$ configuration Tm^{3+}, the same levels are ordered as $^3H_6, ^3H_5, ^3H_4$.

Therefore, the electronic configuration including all terms, levels, and states of Er^{3+}, Tm^{3+}, Yb^{3+} are given below.

Lanthanide	Yb^{3+}	Tm^{3+}	Er^{3+}
Term	1	7	17
Level	2	13	41
State	14	91	364

Also note that for $3 \leq N \leq 11$ there are some ^{2S+1}L terms having the same L and S and, therefore, a sequential index τ, often called seniority quantum number, is added to distinguish these terms, i.e. $^{2S+1}L(\tau)$, defined by group theory introduced by Racah [4] and tabulated by Nielsen and Koster [5].

4f electrons(holes)	13(1)	Yb^{3+}
term : $\|SL\rangle$	1	^{2}F
level : $\|SLJ\rangle$	2	$^2F_{5/2}$, $^2F_{7/2}$
state : $\|SLJM\rangle$	14	J_1: $-\frac{5}{2}, -\frac{3}{2}, -\frac{1}{2}, \frac{1}{2}, \frac{3}{2}, \frac{5}{2}$. J_2: $-\frac{7}{2}, -\frac{5}{2}, -\frac{3}{2}, -\frac{1}{2}, \frac{1}{2}, \frac{3}{2}, \frac{5}{2}, \frac{7}{2}$
4f electrons(holes)	**12(2)**	Tm^{3+}
term : $\|SL\rangle$	7	^{3}H, ^{3}F, ^{1}G, ^{1}D, ^{1}I, ^{3}P, ^{1}S
level : $\|SLJ\rangle$	13	$^3H_6$, $^3F_4$, $^3H_5$, $^3H_4$, $^3F_3$, $^3F_2$, $^1G_4$, $^1D_2$, $^1I_6$, $^3P_0$, $^3P_1$, $^3P_2$, $^1S_0$
state : $\|SLJM\rangle$	91	J_1: $-J_1, \ldots, J_1$. J_2: $-J_2, \ldots, J_2$ ... J_{13}: $-J_{13}, \ldots, J_{13}$
4f electrons(holes)	**11(3)**	Er^{3+}
term : $\|SL\rangle$	17	^{4}I, ^{4}F, ^{4}S, ^{2}H(2), ^{2}G(1), ^{4}G, ^{2}K, ^{2}P, ^{2}D(1), ^{4}D, ^{2}I, ^{2}L, ^{2}H(1), ^{2}D(2), ^{2}F(2), ^{2}G(2), ^{2}F(1)
level : $\|SLJ\rangle$	41	$^4I_{15/2}$, $^4I_{13/2}$, $^4I_{11/2}$, $^4I_{9/2}$, $^4F_{9/2}$, $^4S_{3/2}$, $^2H(2)_{11/2}$, $^4F_{7/2}$, $^4F_{5/2}$, $^4F_{3/2}$, $^2G(1)_{9/2}$, $^4G_{11/2}$, $^4G_{9/2}$, $^2K_{15/2}$, $^2G(1)_{7/2}$, $^2P_{3/2}$, $^2K_{13/2}$, $^4G_{5/2}$, $^2P_{1/2}$, $^4G_{7/2}$, $^2D(1)_{5/2}$, $^2H(2)_{9/2}$, $^4D_{5/2}$, $^4D_{7/2}$, $^2I_{11/2}$, $^2L_{17/2}$, $^4D_{3/2}$, $^2D(1)_{3/2}$, $^2I_{13/2}$, $^4D_{1/2}$, $^2H(1)_{9/2}$, $^2L_{15/2}$, $^2D(2)_{5/2}$, $^2H(1)_{11/2}$, $^2F(2)_{7/2}$, $^2D(2)_{3/2}$, $^2F(2)_{5/2}$, $^2G(2)_{7/2}$, $^2G(2)_{9/2}$, $^2F(1)_{5/2}$, $^2F(1)_{7/2}$
state : $\|SLJM\rangle$	364	J_1: $-J_1, \ldots, J_1$. J_2: $-J_2, \ldots, J_2$ ... J_{41}: $-J_{41}, \ldots, J_{41}$

Figure 1: Term, level, state of Yb^{3+}, Tm^{3+}, Er^{3+}

3.1.2 Spin–Orbit Interaction: $\widehat{H}_{so}$

Spin–orbit interaction results from the interaction of the intrinsic magnetic moment of the electron spin, with the magnetic field created by its motion around its nucleus. While $\widehat{H}_{so}$ is small compared to $\widehat{H}_e$ between the 4f electrons for the light transition metals, it becomes comparable to $\widehat{H}_e$ for the rare earths. As the relative magnitude of the spin-orbit coupling increases, both total spin angular momentum quantum number S and total orbit angular momentum quantum number L are not good quantum numbers anymore, and the total angular momentum J must be introduced.

There are two widely used approaches for angular momentum coupling of L and S to form the total angular momentum J.

- For $\widehat{H}_{so} << \widehat{H}_e$

The $L-S$ coupling(Russel-Saunders) scheme is appropriate where S and L couple separately, i.e. $S = \sum s_i$, $L = \sum l_i$, and the total angular momentum is obtained as $J = L + S$.

- For $\widehat{H}_{so} >> \widehat{H}_e$

The j-j coupling scheme applies where the individual s_i and individual l_i are coupled first, $j_i = s_i + l_i$, and then the total angular momentum is obtained: $J = \sum j_i$.

For rare earths where $\widehat{H}_{so} \approx \widehat{H}_e$, it is known for **intermediate coupling**. Actually, the $L-S$ coupling scheme is commonly used for Ln^{3+}. Because of strong $\widehat{H}_{so}$, the $^{2S+1}$L terms from [Xe] $4f^N$ configuration will further split into several $^{2S+1}L_J$ multiplets with different energies, where $J = |L-S|, |L-S+1|, \ldots, |L+S|$.

3.1.3 Free Ion Approximation

The $^{2S+1}L_J$ multiplets derived above represent the energy levels of the Ln^{3+} ion in the spherical symmetry of free space, the so-called free ions. A further and much smaller energy splitting occurs when the Ln^{3+} ion is placed into the lower symmetry electrostatic field that is produced by the charges of the nearby ions in a solid and external electromagnetic field of laser. Strictly speaking, depending on the exact point symmetry of the electrostatic field at the Ln^{3+} site, a crystal-field splitting occurs, which partially or completely lifts the $(2J+1)$ degeneracy of each $^{2S+1}L_J$ multiplets.

A more complicated investigation shows that independent of the point symmetry of the electric field, odd-electron systems will retain a minimum of two-fold degeneracy in each crystal-field level due to Kramer's degeneracy which can only be lifted by a magnetic field. In contrast, the $(2J+1)$ degeneracy can be completely lifted in even-electron systems by a crystal-field of sufficiently low symmetry. We

will see that crystal-field(CF) and other potential interactions are sometimes indispensable, that can give intensity to the otherwise parity-forbidden 4f $\leftrightarrow$ 4f transitions, and the discrepancy of simulation and experiments can be ascribed to other potential interactions that ignored in our simplified MC model.

Specifically, $|SLJ\rangle$ can be partially or completely lifted by these complex interactions: Stark effect-splitting (electric field of laser or neighboring ions), Zeemann effect-splitting (magnetic field of laser), crystal-field splitting, etc, which are usually only a few hundreds (200 $\sim$ 500) cm^{-1} or a couple of kT (1 kT = 207 cm^{-1} at 298 K), less than most energy level gaps($\Delta E \geq 1000$ cm^{-1}). Hence, the actual population distribution among these micro states of each level can be properly described by the Boltzmann distribution in thermal equilibrium: $z_i = exp(-\frac{\Delta i}{kT})$, where Δi is the energy separation between the ith state and the lowest energy state. However, a more convenient way is to replace the transition matrix element involving the z-component $|SLJM\rangle$ by its average over all z-components of the initial level and final level between two levels $|SLJ\rangle$, thereby dropping the $M = -J, ...J$. Because it has been reported that no detailed knowledge on such fine-structure splitting becomes necessary in the evaluation of the transition probabilities, especially when the splitting is so small. Then, $\frac{z_i}{\sum(z_i)}$ can be replaced by $\frac{1}{2J+1}$. That's why we find the $(2J+1)$ in the denominator of the formulations of ED and MD transition intensity. [6]

Additionally, regarding to the power-density dependent relationship, and the fact that the amplitude of the electric field is proportional to the intensity of the laser beam, it provides a potential perspective that splitting is NOT small at high power density, so the approximation: $\frac{1}{2J+1}$ is not good enough to describe the transition from the state (separated by strong electric field significantly) to others. In summary, different laser power densities may introduce different transition behaviour. Judd-Ofelt theory was originally formulated within the context of $^{2S+1}L_J$ multiplets. Therefore, considering the coordinating environment has only a small influence on the well-shielded 4f electrons, we shall also ignore crystal-field and other complex interactions in the following and simplified the discussion to the transitions between different levels.

3.2 Angular Momentum Coupling of Multi-electron Atoms

In order to construct eigenstate of the multi-electron atoms, the coupling of angular momentum of single electron is required. For example, two 4f electrons, each with a well-defined angular momentum of $l = 3$, interact by electrostatic interaction $\widehat{H}_e$ to form a total angular momentum of the two-electron system. Likewise, the spin and orbital angular momentum of a 4f electron can couple together by spin–orbit interaction $\widehat{H}_{so}$.

3.2.1 Wigner Symbol

The mathematical treatment of coupling two angular momentum gives rise to the so-called Wigner 3-j symbol, which is related to the Clebsch–Gordan(C-G) coefficient [7] and which is given by [8][9]

- Wigner 3-j symbol

$$\begin{pmatrix} a & b & c \\ \alpha & \beta & \gamma \end{pmatrix} = (-1)^{a-b-\gamma}\sqrt{\Delta(a,b,c)}\sqrt{(a+\alpha)!(a-\alpha)!(b+\beta)!(b-\beta)!(c+\gamma)!(c-\gamma)!}\sum_t \frac{(-1)^t}{x(t)} \tag{3}$$

where:

$$x(t) = t!(c-b+t+\alpha)!(c-a+t-\beta)!(a+b-c-t)!(a-t-\alpha)!(b-t+\beta)! \tag{3.1}$$

the sum is taken over all t for which all factorials in $x(t) \geq 0$, and the triangle coefficient $\Delta(a,b,c)$:

$$\Delta(a,b,c) = \frac{(a+b-c)!(a-b+c)!(-a+b+c)!}{(a+b+c+1)!} \tag{3.2}$$

- Wigner 6-j symbol

Coupling three angular momentum gives rise to the so-called Wigner 6-j symbol, which is a sum of products of 3-j symbols. [10][11][12]

$$\left\{ \begin{array}{ccc} j_1 & j_2 & j_3 \\ J_1 & J_2 & J_3 \end{array} \right\} = \sqrt{\Delta\left(j_1, j_2, j_3\right) \Delta\left(j_1, J_2, J_3\right) \Delta\left(J_1, j_2, J_3\right) \Delta\left(J_1, J_2, j_3\right)} \sum_t \frac{(-1)^t (t+1)!}{f(t)} \tag{4}$$

where:

$$\begin{aligned} f(t) = &(t - j_1 - j_2 - j_3)!\,(t - j_1 - J_2 - J_3)!\,(t - J_1 - j_2 - J_3)!\,(t - J_1 - J_2 - 3)! \\ &\times (j_1 + j_2 + J_1 + J_2 - t)!\,(j_2 + j_3 + J_2 + J_3 - t)!\,(j_3 + j_1 + J_3 + J_1 - t)! \end{aligned} \tag{4.1}$$

the sum is taken over all t for which all factorials in $f(t) \geq 0$.

3.2.2 Wigner–Eckart Theorem & Reduced Matrix Elements(RME)

The various interactions in the multi-electron system are described by tensor operators $T_q^{(k)}$, which transform like the spherical harmonics $Y_{k,q}(\theta, \phi)$[13]. The associated theory of tensor operators has been pioneered by Racah. [14][15]

Throughout the calculation of Ln^{3+} energy levels and transition intensities, the need arises to evaluate matrix elements of various tensor operators that act on only one part of the system (say, only the orbital angular momentum or only on the spin).

Application of the Wigner-Eckart theorem [16][17] facilitates the calculation of those matrix elements by making use of so-called **Reduced Matrix Elements(RME)**. The mathematical formulation of this theorem is:

$$\left\langle j' m' \alpha' \left| \mathrm{T}_q^{(k)} \right| j m \alpha \right\rangle = (-1)^{j' - m'} \begin{pmatrix} j' & k & j \\ -m' & q & m \end{pmatrix} \left\langle j' \alpha' || \mathrm{T}^{(k)} || j \alpha \right\rangle \tag{5}$$

where $T_q^{(k)}$ is a tensor operator of rank k whose matrix element is calculated between two states: $\langle j' m' \alpha'|$ and $|jm\alpha\rangle$, with the j', j and m', m being the quantum numbers of the total momentum and their z-components, respectively. All other (if needed) quantum numbers are denoted by α and α'. The double bar entry on the right-hand side is the RME, which depends neither on the magnetic quantum numbers m', m nor on the q-component of the tensor operator $T_q^{(k)}$.

The advantage of the Wigner-Eckart theorem is that any matrix element of a given tensor operator can be calculated in a simple way by multiplying the Wigner 3j-symbol in Eq.(3) with the corresponding RME, which has to be calculated only once for a particular combination of $T_q^{(k)}, j'$, and j.

3.3 RME of Tensor Operators: $\widehat{U}^{(k)}$, $\widehat{V}^{(1x)}$, $\widehat{L} + g\widehat{S}$

Three tensor operators $\widehat{U}^{(k)}$, $\widehat{V}^{(1x)}$, and $\widehat{L} + g\widehat{S}$ and their respective RME are of particular importance for f-electron spectroscopic calculations. Note that the RME of the various tensor operators were calculated in the context of the pure $\left|4f^N SLJ\right\rangle$ wavefunctions, i.e. in the absence of spin-orbit interaction. In real system, a more correct values are evaluated in the intermediate coupling approximation for a specific Ln^{3+}-doped material.

Fitting of the **Barycenter energies**(Section 8.2) to a set of experimental $^{2S+1}L_J$ multiplet energies yields:

- Optimized electrostatic parameters: $F_{(2)}$, $F_{(4)}$, $F_{(6)}$
- Spin-orbit parameter: ζ
- Coefficients c_i of the intermediate coupling wavefunctions (eigenvector of each corresponding eigenvalue)

RME of a tensor operator $\widehat{X}$ between two intermediate coupling wavefunctions $\left|4f^N SLJ\right\rangle'$ and $\left|4f^N S'L'J'\right\rangle'$ is then given by

$$\left\langle l^N SLJ \| \widehat{X} \| l^N S'L'J' \right\rangle' = \sum_i \sum_j c_i c_j \left\langle l^N SLJ \| \widehat{X} \| l^N S'L'J' \right\rangle \tag{6}$$

where the double sum runs over the i and j components of the two intermediate coupling wavefunctions, and the reduced matrix elements $\left\langle l^N SLJ \| X \| l^N S'L'J' \right\rangle$ is any of following equations.

3.3.1 $\widehat{U}^{(k)}$: Electric-dipole Transition Intensities

$$\left\langle l^N SL || \widehat{U}^{(k)} || l^N SL' \right\rangle = N\sqrt{(2L+1)(2L'+1)} \sum_{\psi(l^{N-1})} \left(l^{N-1}\overline{S}L | l^N SL\right) \left\{ \begin{array}{ccc} L & l & \bar{L} \\ l & L' & k \end{array} \right\} (-1)^{\bar{L}+L+l+k} \tag{7}$$

This elegant approach expresses the states of a $4f^N$-electron configuration as linear combinations of the states of the preceding $4f^(N-1)$ electron configuration angular-momentum-coupled to one additional 4f electron [18]. The coefficients of these linear combinations are the coefficients of **fractional parentage**, where the coefficients of fractional parentage is $\left(l^{N-1}\overline{SL} | l^N SL\right)$, calculated by Nielsen and Koster [19] within the definitions of Racah [20].

The conjugate $4f^{14-N}$ electron configuration:

$$\left\langle l^{14-N} SL \| \widehat{U}^{(k)} || l^{14-N} S'L' \right\rangle = -(-1)^k \left\langle l^N SL \left\| \widehat{U}^{(k)} \right\| l^N S'L' \right\rangle \tag{8}$$

Coupling S and L to J then yields [21]:

$$\left\langle l^N SLJ \| \widehat{U}^{(k)} || l^N SL'J' \right\rangle = (-1)^{S+L'+J+k} \sqrt{(2J+1)(2J'+1)} \left\{ \begin{array}{ccc} J & J' & k \\ L' & L & S \end{array} \right\} \left\langle l^N SL \left\| \widehat{U}^{(k)} \right\| l^N SL' \right\rangle \tag{9}$$

For the odd/even rank of this operator, the additional inclusion of the odd-ranked tensors $\lambda = 1, 3, 5$ yielded unphysical results [22]. Then the electric dipole oscillator strength is given as:

$$f_{ED}^{abs} = \frac{8\pi^2 m_e}{3h} \frac{v}{(2J+1)} \frac{\chi_{ED}^{abs}}{n} \sum_{\lambda=2,4,6} \Omega_{(\lambda)} \left| \left\langle l^N SLJ || \widehat{U}^{(k)} || l^N S'L'J' \right\rangle \right|^2 \tag{10}$$

3.3.2 $\widehat{V}^{(1x)}$: RME of Spin-Orbit Interaction Operator $\widehat{H}_{so}$

$$\left\langle l^N SL || \widehat{V}^{(1x)} || l^N S'L' \right\rangle = N\sqrt{s(s+1)(2s+1)(2S+1)(2L+1)(2S'+1)(2L'+1)} \quad \times \text{SUM} \tag{11}$$

where

$$\text{SUM} = \sum_{\psi(l^{N-1})} \left(l^{N-1}\overline{S}L \; | l^N SL\right) \left\{ \begin{array}{ccc} S & S' & 1 \\ s & s & \bar{S} \end{array} \right\} \left\{ \begin{array}{ccc} L & L' & x \\ l & l & \bar{L} \end{array} \right\} (-1)^{\bar{S}+\bar{L}+S+L+s+l+x+1} \tag{11.1}$$

For 4f-electron, $s = 1/2, l = 3$, and the matrix elements of $\widehat{H}_{so}$ are given as:

$$\left\langle 4f^N SLJ \left| \widehat{H}_{so} \right| 4f^N S'L'J' \right\rangle = \zeta(-1)^{J+L+S'} \sqrt{l(l+1)(2l+1)} \left\{ \begin{array}{ccc} S & S' & 1 \\ L' & L & J \end{array} \right\} \left\langle l^N SL \left\| \widehat{V}^{(1x)} \right\| l^N S'L' \right\rangle \tag{12}$$

For the conjugate $4f^{14-N}$ electron configuration:

$$\langle l^{14-N} SL || \widehat{V}^{(1x)} || l^{14-N} S'L' \rangle = (-1)^x \left\langle l^N SL \left\| \widehat{V}^{(1x)} \right\| l^N S'L' \right\rangle \tag{13}$$

3.3.3 $\widehat{L}+g\widehat{S}$: Magnetic-dipole Transition Intensity

- When $J'=J$

$$\left\langle l^N SLJ||\widehat{L}+g\widehat{S}||l^N SLJ'\right\rangle = g\sqrt{J(J+1)(2J+1)} \tag{14}$$

- When $J'=J-1$

$$\left\langle l^N SLJ||\widehat{L}+g\widehat{S}||l^N SL(J-1)\right\rangle = (g-1)\sqrt{\frac{(S+L+J+1)(J+L-S)(J+S-L)(S+L-J+1)}{4J}} \tag{15}$$

- When $J'=J+1$

$$\left\langle l^N SLJ\|\widehat{L}+g\widehat{S}\|l^N S'L'(J+1)\right\rangle = (g-1)\sqrt{\frac{(S+L+J+2)(S+L-J)(L+J-S+1)(J+S-L+1)}{4(J+1)}} \tag{16}$$

The magnetic-dipole transition intensity is given as:

$$A^{MD}_{SLJ\to S'L'} = \frac{\pi h e^2}{3\varepsilon_0 c^5 m_e^2}\frac{v^3}{(2J+1)}n^3\left|\left\langle l^N SLJ||\widehat{L}+g\widehat{S}||l^N SLJ'\right\rangle\right|^2 \tag{17}$$

where the g-factor of the electron: $g=2.002319304362$.

3.4 Intermediate Coupling Scheme and Eigenvalues

3.4.1 RME of Electrostatic Operator $\widehat{H}_e$

The Hamilton operator for the electrostatic interaction is:

$$\widehat{H}_e = \frac{e^2}{r_{ij}} \propto \sum_{k=0,2,4,6} C_i^{(k)} C_j^{(k)} \tag{18}$$

where the expansion is in terms of the tensor operators:

$$C_q^{(k)} = \sqrt{4\pi/(2k+1)}Y_{kq} \tag{19}$$

which is a function of the spherical harmonics Y_{kq}. The matrix elements of $\widehat{H}_e$ are then given by:

$$\begin{aligned}\left\langle l^N SL\left|C_i^{(k)}\cdot C_j^{(k)}\right|l^N S'L'\right\rangle &= \delta_{SS'}\delta_{LL'}(-1)^{4l}(-1)^L(2l+1)^2 \\ &\times \sum_{k=0,2,4,6}\begin{pmatrix} l & k & l \\ 0 & 0 & 0\end{pmatrix}^2\begin{Bmatrix} l & l & k \\ l & l & L\end{Bmatrix}F_{(k)}\end{aligned} \tag{20}$$

which for f-electron ($l=3$) becomes:

$$\begin{aligned}\left\langle 4\mathrm{f}^N SL\left|C_i^{(k)}\cdot C_j^{(k)}\right|4f^N S'L'\right\rangle &= \delta_{SS'}\delta_{LL'}49(-1)^L \\ &\times \sum_{k=0,2,4,6}\begin{pmatrix} 3 & k & 3 \\ 0 & 0 & 0\end{pmatrix}^2\begin{Bmatrix} 3 & 3 & k \\ 3 & 3 & L\end{Bmatrix}F_{(k)}\end{aligned} \tag{20.1}$$

The $\left\langle 4f^N SL\right|$ and $\left|4f^N S'L'\right\rangle$ are the two interacting states, and the $F_{(k)}$ are the **Slater integrals**. (The sum is limited to $k=0,2,4,6$, for all other k the 3j and/or 6j symbols are zero). Since $\widehat{H}_e$ is an electric interaction it cannot act on the spin [23], and therefore the matrix element is zero if $S\neq S'$ and $L\neq L'$, as denoted by the Kronecker $\delta_{SS'}$ and $\delta_{LL'}$, respectively.

There are also two notations $F_{(k)}$ and $F^{(k)}$ for the Slater integrals commonly found in the literature, and the respective conversions are:

$$\begin{aligned} F_{(0)} &= F^{(0)} \\ F_{(2)} &= F^{(2)}/225 \\ F_{(4)} &= F^{(4)}/1089 \\ F_{(6)} &= 25F^{(6)}/184041 \end{aligned} \tag{20.2}$$

For these $4f^N$ electron configurations with $3 \leq N \leq 11$ there are some ^{2S+1}L terms with the same L and S which are distinguished by an additional sequential index τ, which produces off-diagonal matrix elements. This problem was solved by Nielsen and Koster [24] who have applied the respective classification of states by Racah [25] and have consistently tabulated all electrostatic matrix elements for all $4f^N$ electron configurations in the form:

$$\left\langle 4f^N SL \left| \widehat{H}_e \right| 4f^N S'L' \right\rangle = \sum_{k=0}^{3} e_k E^{(k)} \tag{21}$$

where:

- e_k: Tabulated coefficients [26]
- $E^{(k)}$: related to the Slater integrals:

$$\begin{aligned} E^{(0)} &= F_{(0)} - 10F_{(2)} - 33F_{(4)} - 286F_{(6)} \\ E^{(1)} &= \left(70F_{(2)} + 231F_{(4)} + 2002F_{(6)}\right)/9 \\ E^{(2)} &= \left(F_{(2)} - 3F_{(4)} + 7F_{(6)}\right)/9 \\ E^{(3)} &= \left(5F_{(2)} + 6F_{(4)} - 91F_{(6)}\right)/3 \end{aligned} \tag{21.1}$$

Given a set of Slater integrals $F_{(2)}, F_{(4)}, F_{(6)}$, the matrix elements of $\widehat{H}_e$ can now be evaluated. Additionally, $F_{(0)}$ Slater integral is usually omitted as it simply produces a uniform shift of the energies of all the states of the configuration, which is irrelevant when the energies are reference to the ground-state multiplet of the $[Xe]4f^N$ electron configuration. [27]

3.4.2 RME of Spin-Orbital Interaction Operator $\widehat{H}_{so}$

The Hamilton operator for the spin-orbit interaction is: [28]

$$\widehat{H}_{so} = \sum_{i=1}^{N} \xi\left(r_i\right)\left(\mathrm{s}_i \cdot \mathrm{l}_i\right) \tag{22}$$

where:

- r_i: The radial coordinate of the ith electron
- s_i and l_i: The spin and orbital angular momentum
- $\xi\left(r_i\right) = \dfrac{\hbar^2}{m^2c^2r_i}\dfrac{U(r_i)}{dr_i}$
- $U\left(r_i\right)$: The central field potential (Central Field Approximation) [29]

The spin-orbit interaction is not diagonal in the basis set of $\widehat{L}$ and $\widehat{S}$ used in the $L-S$ coupling scheme, and $\widehat{H}_{so}$ will therefore contribute off-diagonal elements to the $\widehat{H}$-matrix in Eq.(27), and $\widehat{H}_{so}$ mixes all states that have the same J. The matrix elements of $\widehat{H}_{so}$ are then given by:

$$\left\langle 4f^N SLJ \left| \widehat{H}_{so} \right| 4f^N S'L'J' \right\rangle = \zeta(-1)^{J+L+S'} \sqrt{l(l+1)(2l+1)} \times \left\{ \begin{array}{ccc} S & S' & 1 \\ L' & L & J \end{array} \right\} \left\langle l^N SL \left\| \widehat{V}^{(1x)} \right\| l^N S'L' \right\rangle \tag{23}$$

$l = 3$ for $4f$ electrons, and ζ is the spin–orbit coupling parameter which is a constant for all electronic configurations in a given material(e.g. $NaYF_4$), while the RME of $\widehat{V}^{(1x)}$ tensor operator of the spin–orbit interaction can be found in Eq.(11).

3.4.3 Eigenvalue equation $\widehat{H} = \widehat{H}_e + \widehat{H}_{so}$

From free ion approximation mentioned before, $^{2S+1}L_J$ is derived in free space, so these ions are free ions, but what if we put these ions into a crystal with periodic structure?

Firstly, energy level will be further splitted and there is a **barycenter energy**(Section 8.2). Crystal-field splitting occurs depending on the exact point symmetry of the electrostatic field at the Ln^{3+} site**(Local Site Symmetry)**. Secondly, because of the crystal-field interactions(C-F), essential ingredient that gives intensity to the otherwise parity-forbidden 4f↔4f transitions.

Detailed studies of C-F interactions in Ln^{3+}-doped solids have shown that the combined magnitude of $\widehat{H}_e$ and $\widehat{H}_{so}$ amounts to 80%-90% of all interactions. Therefore, $\widehat{H}_e$ and $\widehat{H}_{so}$ are dominant in Ln^{3+} ions. In the context of the J-O theory, considering only $\widehat{H}_e$ and $\widehat{H}_{so}$ offers a useful first-order description known as the intermediate coupling approximation.

The other 10%–20% are due to higher-order atomic such as inter-configurational interactions, two-body spin–orbit interactions, etc. These higher-order contributions are important if a quantitative description of crystal-field energy levels and transitions between them is sought. Tanner and Duan have given a comprehensive analysis of the crystal-field and free-ion parameters for the entire series of rare-earth ions doped into $Cs_2NaLnCl_6$, and they presented linear and quadratic fits of the electrostatic $\left(F_{(2)}, F_{(4)}, F_{(6)}\right)$ and spin-orbit (ζ) interaction parameters as a function of the number of 4f electrons. [30]

- Schrodinger's equation

In this approximation, the total Hamilton operator of the system:

$$\widehat{H} = \widehat{H}_e + \widehat{H}_{so} \tag{24}$$

The energies(eigenvalues) of the respective $^{2S+1}L_J$ multiplets are then found by solving the time-independent Schrödinger equation:

$$\widehat{H}\Psi = E\Psi \tag{25}$$

where $\Psi = (\Psi_1, \ldots, \Psi_z)$ represents there are totally z different $^{2S+1}L_J$ multiplets of the 4f electron configuration. The dimensions of the $\widehat{H}$ matrix is $z \times z$:

$$\widehat{H} = \begin{bmatrix} \widehat{H}_{11} & \widehat{H}_{12} & \cdots & \widehat{H}_{1z} \\ \widehat{H}_{21} & \widehat{H}_{22} & \cdots & \widehat{H}_{2z} \\ \vdots & \vdots & \ddots & \vdots \\ \widehat{H}_{z1} & \widehat{H}_{z2} & \cdots & \widehat{H}_{zz} \end{bmatrix} \tag{26}$$

The matrix form of the intermediate coupling eigenvalue equation:

$$\begin{bmatrix} \widehat{H}_{11} & \widehat{H}_{12} & \cdots & \widehat{H}_{1z} \\ \widehat{H}_{21} & \widehat{H}_{22} & \cdots & \widehat{H}_{2z} \\ \vdots & \vdots & \ddots & \vdots \\ \widehat{H}_{z1} & \widehat{H}_{z2} & \cdots & \widehat{H}_{zz} \end{bmatrix} \begin{bmatrix} \Psi_1 \\ \Psi_2 \\ \vdots \\ \Psi_z \end{bmatrix} = E \begin{bmatrix} \Psi_1 \\ \Psi_2 \\ \vdots \\ \Psi_z \end{bmatrix} \tag{27}$$

where each matrix element is given by $\widehat{H}_{ij} = \widehat{H}_e^{(ij)} + \widehat{H}_{so}^{(ij)}$ and the matrix is square $(z \times z)$ and symmetrical, i.e. $\widehat{H}_{ij} = \widehat{H}_{ji}$. The eigenvalue equation is solved by calculating each matrix element $\widehat{H}_{ij}$ of the Hamiltonian matrix $\widehat{H}$:

$$\langle i|\widehat{H}|f\rangle = \left\langle i\left|\widehat{H}_e + \widehat{H}_{so}\right|f\right\rangle = \left\langle i\left|\widehat{H}_e\right|f\right\rangle + \left\langle i\left|\widehat{H}_{so}\right|f\right\rangle \tag{28}$$

Then diagonalizing the matrix to obtain both the energies as the corresponding eigenvalues and the coefficients c_i of the intermediate coupling wavefunctions.

- Matrix diagonalizing

We are now in a position to calculate the matrix elements of $\widehat{H} = \widehat{H}_e + \widehat{H}_{so}$ using Eq.(21) and Eq.(23). In the basis set of $\left|4f^N SLJ\right\rangle$, the $\widehat{H}$-matrix has off-diagonal elements that arise from: (1) Mixing of different states with the same J by spin-orbit coupling. (2) Mixing of states with the same S and L by electrostatic interaction

There is no fundamental obstacle in calculating all energies, given a set of material-specific $F_{(k)}$ and ζ parameters of $NaYF_4$. Numerical diagonalization of the square symmetric $\hat{H}$-matrix solves this eigenvalue problem and yields the wavefunctions and energies of each $\left|4f^N SLJ\right\rangle$ multiplet, which is expressed as a linear combination of all other states in the configuration having the same J and being mixed by spin-orbit interaction, i.e.

$$\left|4f^N SLJ\right\rangle = \sum_i c_i \left|4f^N S'L'J\right\rangle \tag{29}$$

where $\sum c_i^2 = 1$ and J are the same in mixed wave functions. Note that $\left|4f^N SLJ\right\rangle$ wavefunction is not the pure $\left|4f^N SLJ\right\rangle$ wavefunction anymore. Such a strong mixture of these states induced by the spin–orbit interaction. Consider RME of a tensor operator $\widehat{X}$ between two intermediate coupling wavefunctions $|4f^N SLJ\rangle$ and $|4f^N S'L'J'\rangle$:

$$\begin{aligned} \left|4f^N SLJ\right\rangle &= \sum_i c_i \left|4f^N S_a L_a J\right\rangle \\ \left|4f^N S'L'J'\right\rangle &= \sum_j c_j \left|4f^N S'_b L'_b J'\right\rangle \end{aligned} \tag{29.1}$$

$$\Rightarrow \left\langle l^N SLJ|\mathrm{X}|l^N S'L'J'\right\rangle = \sum_i \sum_j c_i c_j \left\langle l^N S_a L_a J|\mathrm{X}|l^N S'_b L'_b J'\right\rangle \tag{29.2}$$

Where $\widehat{X}$ could be: $\widehat{U}^{(k)}$, $\widehat{V}^{(1x)}$, $\widehat{L}+g\widehat{S}$. For the coefficients c_i, see more details in Section 8.2 about experiments fitting of the Barycenter energies to a set of experimental $^{2\ S+1}L_J$ multiplet energies:

$$E_B\left(^{2\ S+1}L_J\right) = \frac{1}{2J+1}\sum_i g_i E_i \tag{30}$$

For example, the pure $^4I_{9/2}$ wavefunction of $Er^{3+}\left(4f^{11}\right)$:

$$\begin{aligned} \left|^4\mathrm{I}_{9/2}\right\rangle' = &-0.4083\left|^4\ \mathrm{F}_{9/2}\right\rangle - 0.02023\left|^4\mathrm{G}_{9/2}\right\rangle \\ &+ 0.6731\left|^4\ \mathrm{I}_{9/2}\right\rangle - 0.3122\left|^2\ \mathrm{G}(1)_{9/2}\right\rangle + 0.2521\left|^2\ \mathrm{G}(2)_{9/2}\right\rangle \\ &- 0.2080\left|^2\ \mathrm{H}(1)_{9/2}\right\rangle + 0.4190\left|^2\ \mathrm{H}(2)_{9/2}\right\rangle \end{aligned} \tag{31}$$

As a result, the actual $\left|^4\mathrm{I}_{9/2}\right\rangle'$ wavefunction only retains $(0.6731)^2$, i.e. 45.3% of its $\left|^4\mathrm{I}_{9/2}\right\rangle$ origin as a result of spin-orbit coupling. All the other $J = 9/2$ multiplets of the $4f^{11}$ configuration are admixed to various degrees. Different components contribute differently.

4 Transitions Intensity of Lanthanide in Solids

4.1 Transitions of 4f Electronic Configurations

The probability for a transition from Ψ_1 to Ψ_2 to take place is proportional to the transition moment:

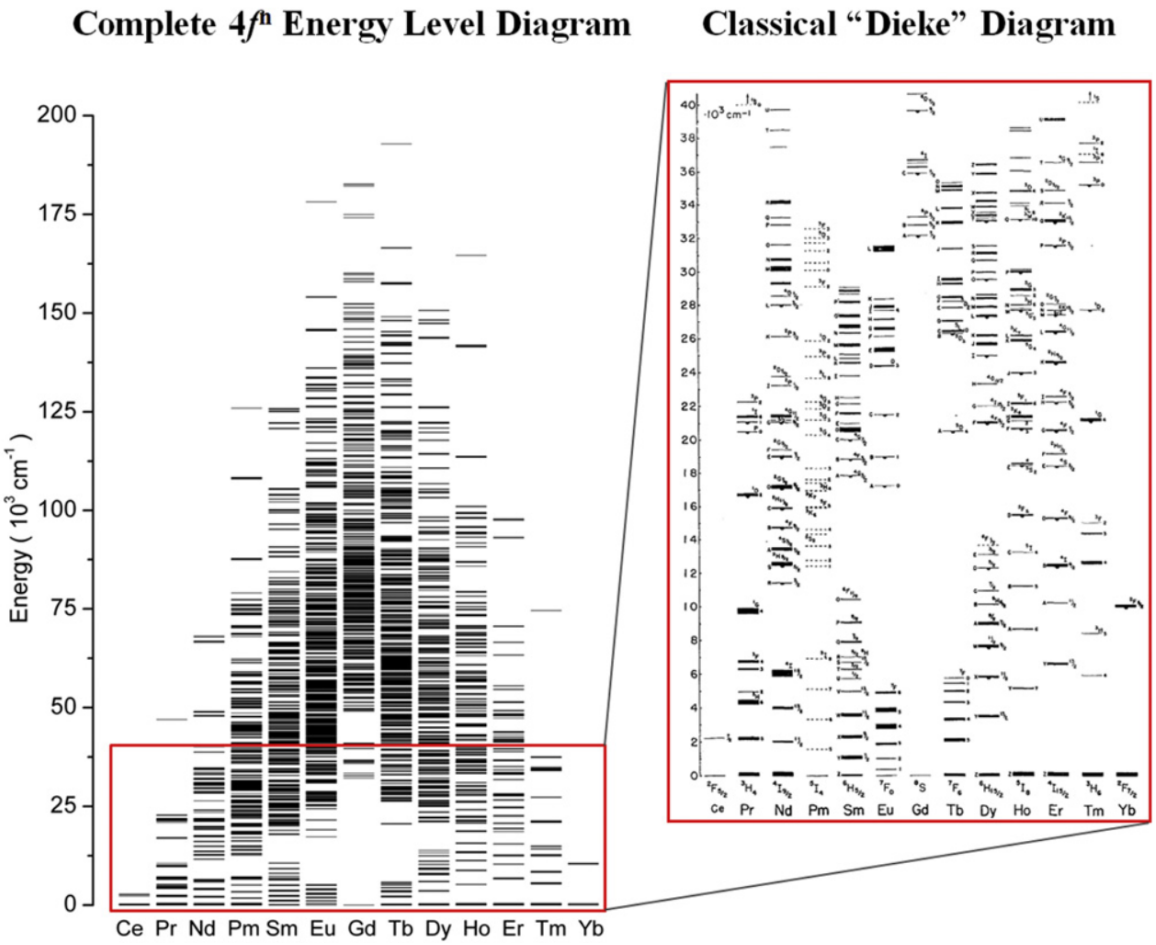

Figure 2: Energy levels of the $^{2S+1}L_J$ multiplets of all Ln^{3+} ions, results from $\widehat{H}_e$ and $\widehat{H}_{so}(80\% \sim 90\%)$. Left: Calculated diagram of $^{2S+1}L_J$ multiplets for each Ln^{3+} ion [31]. Right: The classical Dieke diagram [32] compiled in the 1960s experimentally, with energies up to $40,000$ cm^{-1}, a range that is accessible in typical optical spectroscopy experiments.

$$\vec{M}_{12} = \int \Psi_2 \vec{\mu} \Psi_1 d\tau \tag{32}$$

where $\vec{\mu}$ is the dipole moment operator. The integral above is non-zero only if the direct product of $\Psi_2 \otimes \vec{\mu} \otimes \Psi_1$ is symmetric **(gerade)** with respect to the center of symmetry (also known as Laporte selection rule). The exchange of energy between an electromagnetic field(laser) and the electrons of an atom is generally dominated by electric-dipole (ED) interactions, and the electric-dipole operator has ungerade (u) inversion symmetry. Likewise, the 4f wavefunctions have ungerade (u) inversion symmetry. Hence, for an ED-induced 4f $\leftrightarrow$ 4f transition, the direct product is $u \otimes u \otimes u = u$, and the transition has zero probability because the integral vanishes. [33]

In order for ED-induced 4f $\leftrightarrow$ 4f transitions to occur at all, some admixture of states with opposite, i.e. gerade, parity into the 4f wavefunctions is required. In a solid, such admixtures can be mediated by odd-parity crystal-field components (giving rise to electronic transitions) as well as odd-parity vibrations (giving rise to vibronic transitions)[34]. This is the fundamental premise of the J-O theory.

The formalism begins by admixing even-parity states φ_{nl} into the pure 4f wavefunction $\left|\mathrm{f}^N J M_J\right\rangle$ via an odd-parity crystal field in order to obtain a new wavefunction $|B\rangle$:

$$|B\rangle = \left|\mathrm{f}^N J M_J\right\rangle + \frac{\sum_{\varphi_{nl}} \left\langle \left(\left\langle \mathrm{f}^N J M_J | \widehat{V} | \varphi_{nl} \right\rangle \right) \mid \varphi_{nl} \right\rangle}{E\left(\mathrm{f}^N J M_J\right) - E\left(\varphi_{nl}\right)} \tag{33}$$

where $E\left(\mathrm{f}^N J M_J\right) - E\left(\varphi_{nl}\right)$ is the energy differences and the several perturbing even-parity states φ_{nl}. $\widehat{V}$ is the crystal-field interaction operator. For a transition between two 4f states $B \rightarrow B'$ and using the admixed wavefunctions, the matrix element of the electric dipole(ED) moment is given by [1],

$$\begin{aligned} \left\langle B \left| \mathrm{D}_q^{(k)} \right| B' \right\rangle = \sum_{\varphi_{nl}} \Bigg\{ & \frac{\left\langle \mathrm{f}^N J M_J \right| \mathrm{V} | \varphi_{nl} \rangle \left\langle \mathrm{f}^N J' M'_J \left| \mathrm{D}_q^{(k)} \right| \varphi_{nl} \right\rangle}{E\left(\mathrm{f}^N J M_J\right) - E\left(\varphi_{nl}\right)} \\ & + \frac{\left\langle \mathrm{f}^N J' M'_J | \mathrm{V} | \varphi_{nl} \right\rangle \left\langle \mathrm{f}^N J M_J \left| \mathrm{D}_q^{(k)} \right| \varphi_{nl} \right\rangle}{E\left(\mathrm{f}^N J' M'_J\right) - E\left(\varphi_{nl}\right)} \Bigg\} \end{aligned} \tag{34}$$

There are two assumptions:

- First, it is assumed that all sublevels of a given even-parity state φ_{nl} are degenerate. This is a rather drastic assumption when compared to typical $4\mathrm{f}^{\mathrm{N}} - 4\mathrm{f}^{\mathrm{N}-1}5$ d separations, because actual crystal-field splittings of the $4\mathrm{f}^{\mathrm{N}-1}5$ d states for example are on the order of $5000 \sim 30,000$ cm^{-1}. [35]
- Second, it is assumed that $E\left(\mathrm{f}^N J M_J\right) - E\left(\varphi_{nl}\right) = E\left(\mathrm{f}^N J' M'_J\right) - E\left(\varphi_{nl}\right)$. This is also a rough assumption because the $4\mathrm{f}^{\mathrm{N}} - 4\mathrm{f}^{\mathrm{N}-1}5$ d separation is within a factor of $2 \sim 10$ of typical 4f $\leftrightarrow$ 4f transition energies. [36]

With these assumptions, however, it is possible to combine the two sums in Eq.(34) and to simplify the matrix element of the electric-dipole(ED) moment to a sum of only three terms, expressed as oscillator strength. Actually the fact that the transition strength can be expanded as the sum of three even-ranked tensors is one of the key results of J-O theory. [37]

4.2 ED Oscillator Strengths

The intensity of the ED-induced absorption $\left|l^N S L J\right\rangle \rightarrow \left|l^N S' L' J'\right\rangle$ then becomes:

$$f_{ED}^{abs} = \frac{8\pi^2 m_e}{3h} \frac{v}{(2J+1)} \frac{\chi_{ED}^{abs}}{n} \sum_{\lambda=2,4,6} \Omega_{(\lambda)} \left| \left\langle l^N S L J || \widehat{U}^{(\lambda)} || l^N S' L' J' \right\rangle \right|^2 \tag{35}$$

where:

- $\Omega_{(\lambda)}$ (cm^2): Three Judd-Ofelt intensity parameters

- ν (s^{-1}): Mean transition frequency
- n: Refractive index at the transition frequency ($\nu = \frac{c}{\lambda}$)s^{-1}
- χ_{ED}^{abs}: Localfield correction (only for ED)

4.3 MD Oscillator Strengths

The oscillator strength for a magnetic-dipole (MD) induced absorption $\left|l^N SLJ\right\rangle \rightarrow \left|l^N SLJ'\right\rangle$ only depends on one reduced matrix element $\left\langle l^N SLJ||\widehat{L}+g\widehat{S}||l^N SLJ'\right\rangle$. Unlike ED-transitions, it has no intensity scaling parameter and is given by: [38]

$$f_{MD}^{abs} = \frac{hv}{6m_e c^2}\frac{n}{(2J+1)}\left|\left\langle l^N SLJ\|\widehat{L}+g\widehat{S}\|l^N SLJ'\right\rangle\right|^2 \tag{36}$$

There is no need for a local-field correction for magnetic fields in nonmagnetic materials, i.e. $H_{\text{loc}}/H = 1$. [39]

Some transitions have both ED and MD contributions, and the total oscillator strength is then given by:

$$f^{abs} = f_{ED}^{abs} + f_{MD}^{abs} \tag{37}$$

4.4 χ_{ED}^{abs}: Local Field Correction

The factor χ in Eq.(35) takes into account that the local electric field E_{loc}, at the site of the ion undergoing an optical transition is generally different from the macroscopic field E in the medium. Several models for this local-field correction have been proposed in the past. [40]

- Virtual-Cavity model(Lorentz model)

The virtual-cavity model (Lorentz model) is a reasonable approximation for Ln^{3+} ions doped into a solid such as a crystal or glass, while other models have been proposed for nano-particles embedded in a medium. The local-field correction for an ED-induced absorption is given by:

$$\chi_{ED}^{abs} = [E_{loc}/E]^2 = \left(\frac{n^2+2}{3}\right)^2 \tag{38}$$

in the virtual-cavity model, which also shows that the oscillator strength is proportional to the square of the electric field. The additional factor of $1/n$ in Eq.(35) is often combined with χ_{ED}^{abs} even though it has a different physical origin, here is a brief interpretation.

Note that the virtual cavity model is strictly only valid for cubic symmetry and for equal polarizability of the Ln^{3+} ion and the medium [41]. (Most studies implicitly use the virtual-cavity model and the associated localfield correction shown above). Deviations from this ideal case would require more complex descriptions of the local electric field [42]. In some systems, the empty cavity model with $\chi_{ED}^{abs} = [E_{loc}/E]^2 = \left(\frac{3n^2}{2n^2+1}\right)^2$ was found to provide a better description. [43][44].

The photon flux in vacuum is $\Phi_0 = \left(c^2/4\pi\right)E_0^2$, while in a dielectric medium it is $\Phi_m = (v/4\pi)n^2E_0^2 = n(c/4\pi)E_0^2$ with $v = c/n$. Since the photon flux does not change upon entering the dielectric medium from the vacuum, an additional factor of $1/n$ has to be included in the expression of the ED oscillator strength, so that $\Phi_0 = \Phi_m$. [45]

4.5 Refractive Index Dispersion of Materials(Sellmeier Equation)

Another complication is the refractive index dispersion of materials. It is often ignored and a fixed refractive index such as the index n_D at the sodium D-line (589.3 nm) is used independent of the wavelength λ of the transition. This can be problematic for transitions near the band gap energy of the material where the refractive index can easily be up to 30% greater than n_D. It is desirable to include dispersion for example by describing the refractive index with the Sellmeier equation: [46]

$$n(\lambda)^2 = 1 + \sum_{i=1}^{3} \frac{B_i \lambda^2}{\lambda^2 - C_i} \tag{39}$$

where B_i and C_i are phenomenological material constants that are typically obtained from a fit of Eq.(39) to a number of refractive index measurements at different wavelengths λ. The situation is further complicated in anisotropic crystals that have more than one characteristic refractive index. In uniaxial crystals, taking the average of the ordinary and extraordinary refractive index is a good approximation as long as the birefringence is not too large. [47]

Finally, the above ED and MD-induced absorption oscillator strengths have to be multiplied by n^2 for the case of emission. [48]

- The intensity of the ED emission $\left|l^N SLJ\right\rangle \rightarrow \left|l^N S'L'J'\right\rangle$(ED oscillator strengths)

$$f_{ED}^{emi} = n^2 \times f_{ED}^{abs} = \frac{8\pi^2 m_e}{3h} \frac{v}{(2J+1)} n\chi_{ED}^{abs} \sum_{\lambda=2,4,6} \Omega_{(\lambda)} \left|\left\langle l^N SLJ||\widehat{U}^{(\lambda)}||l^N S'L'J'\right\rangle\right|^2 \tag{40}$$

- The intensity of the MD emission $\left|l^N SLJ\right\rangle \rightarrow \left|l^N S'L'J'\right\rangle$(MD oscillator strengths)

$$f_{MD}^{emi} = n^2 \times f_{MD}^{abs} = \frac{h\upsilon}{6m_e c^2} \frac{n^3}{(2J+1)} \left|\left\langle l^N SLJ\|\widehat{L} + g\widehat{S}\|l^N S'L'J'\right\rangle\right|^2 \tag{41}$$

5 Derived Quantities

5.1 Electric-dipole Transition

The selection rule of electric-dipole induced transition: $\Delta l = \pm 1, \Delta S = 0, \Delta L \leq 2l, \Delta J \leq 2l (l = 3)$(forbidden: $0 \rightarrow 0$). For an electric-dipole transition $\left|l^N SLJ\right\rangle \rightarrow \left|l^N S'L'J'\right\rangle$, the rate of spontaneous radiative decay $A_{SLJ \rightarrow S'L'J'}^{ED}$ is given by:

$$A_{SLJ \rightarrow S'L'J'}^{ED} = \frac{8\pi h\upsilon^3}{c^3} B_{SLJ \rightarrow S'L'J'}^{ED} \tag{42}$$

here the Einstein coefficient:

$$B_{SLJ \rightarrow S'L'J'}^{ED} = \frac{e^2}{4hm_e \varepsilon_0 \upsilon} f_{ED}^{emi} \tag{43}$$

where f_{ED}^{emi} is given above.

5.1.1 Comparison with Emory's Model

Original paper: [49].

$$S_{ij}^{\mathrm{ED}} = \sum_{\lambda=2,4,6} \Omega_\lambda \left|\left\langle [\mathrm{SL}] J_i \left\| \widehat{U}^{(\lambda)} \right\| [\mathrm{SL}] J_j \right\rangle\right|^2 \tag{44}$$

Therefore,

$$A_{SLJ \rightarrow S'L'J'}^{ED} = \frac{16\pi^3 e^2}{3\varepsilon_0 hc^3} \frac{\upsilon^3}{(2J+1)} n\chi_{ED}^{emi} S_{ij}^{\mathrm{ED}} \tag{45}$$

The fundamental constants are given in SI units. However, in Emory's model, the local-field correction χ_{ED}^{emi} is chosen as:

$$\chi_{ED}^{abs} = (\frac{n^2+2}{3})^2 = \frac{(n^2+2)^2}{9} \tag{46}$$

Elementary charge: $e_{cgs} = 4.8 \times 10^{-10} g^{1/2} \cdot cm^{3/2} \cdot s^{-1}$ (Gaussian Units)

Hence, $e_{cgs} = e_{SI} \times \frac{1}{\sqrt{4\pi\varepsilon_0}}$, and $e^2_{cgs} = e^2_{SI} \times \frac{1}{4\pi\varepsilon_0}$

$$A^{ED}_{SLJ\to S'L'J'} = \frac{16\pi^3 e^2_{SI}}{3\varepsilon_0 hc^3}\frac{v^3}{(2J+1)} n\chi^{abs}_{ED} S^{\mathrm{ED}}_{ij} \tag{47}$$

$\Rightarrow$

$$A^{ED}_{SLJ\to S'L'J'} = \frac{16\pi^3 e^2_{SI} \times \frac{1}{4\pi\varepsilon_0} \times 4\pi\varepsilon_0}{3\varepsilon_0 hc^3}\frac{v^3}{(2J+1)} n\frac{(n^2+2)^2}{9} S^{\mathrm{ED}}_{ij} \tag{48}$$

$\Rightarrow$

$$A^{ED}_{SLJ\to S'L'J'} = \frac{16\pi^3 e^2_{cgs} \times 4\pi\varepsilon_0}{3h\varepsilon_0}\frac{v^3}{c^3}\frac{1}{(2J+1)} n\frac{(n^2+2)^2}{9} S^{\mathrm{ED}}_{ij} \tag{49}$$

$\Rightarrow$

$$A^{ED}_{SLJ\to S'L'J'} = \frac{64\pi^4 e^2_{cgs}\widetilde{\nu}^3}{3h(2J+1)}\left[\frac{n(n^2+2)^2}{9}\right] S^{\mathrm{ED}}_{ij} \tag{50}$$

- $\widetilde{\nu}$ energy of the transition in wavenumbers (cm^{-1})
- $S^{\mathrm{ED}}_{ij} = \sum_{\lambda=2,4,6} \Omega_\lambda \left|\left\langle [\mathrm{SL}]J_i \left\| U^{(\lambda)} \right\| [\mathrm{SL}]J_j \right\rangle\right|^2$

Note: implicit in the $(2J+1)$ degeneracy factor in above equations is the assumption that all levels of the initial J multiplet are equally populated or that transitions from all crystal-field levels of the multiplet are equally probable.

5.1.2 Comparison with Weber's Model

Original paper: [50].

$$A_{\mathrm{ed}}\left([\alpha SL]J;[\alpha' S'L']\,J'\right) = \frac{8\pi^2 e^2 n^2 \nu^3}{mc^3(2J+1)} \sum_{\lambda=2,4,6} T_\lambda \left\langle 4f^N[\alpha SL]J \left\| \widehat{U}^{(\lambda)} \right\| 4f^N\left[\alpha' S'L'\right]J' \right\rangle^2 \tag{51}$$

where

- $T_\lambda = \frac{8\pi^2 m}{3h}\frac{(n^2+2)^2}{9n}\Omega_\lambda$
- Ω_λ: Judd-Ofelt intensity parameters / Phenomenological intensity parameters depend on both the host lattice and the species of the rare earth ion, where $\lambda = 2, 4, 6$
- n: Refractive index
- m (g): Electron mass
- e ($\mathrm{g}^{1/2}\cdot\mathrm{cm}^{3/2}\cdot\mathrm{s}^{-1}$): Elementary charge
- ν (s^{-1}): Transition frequency
- h ($\mathrm{g}\cdot\mathrm{cm}^2\cdot\mathrm{s}^{-1}$): Planck constant

5.1.3 Comparison with Takash's Model

Original paper: [51].

$$W\left(J_a \to J'_a\right) = \frac{4e^2\omega^3_{aa'}}{3\hbar c^3}\chi_{\mathrm{ed}}\frac{1}{2J_a+1}\sum_\lambda \Omega_\lambda \left\langle J_a \left\| U^{(\lambda)} \right\| J_{a'} \right\rangle^2 \tag{52}$$

where

- $\hbar = \dfrac{h}{2\pi}$
- h ($\mathrm{g \cdot cm^2 \cdot s^{-1}}$): Planck constant
- $\omega_{aa'} = 2\pi\nu$: Angular frequncy
- ν ($\mathrm{s^{-1}}$): Transition frequency
- $\widetilde{\nu} = \dfrac{1}{\lambda} = \dfrac{\nu}{c}\mathrm{cm^{-1}}$: Wave number
- $\chi_{\mathrm{ed}} = \dfrac{n(n^2+2)^2}{9}$: local field correction.
- Ω_λ ($\mathrm{cm^2}$): Judd-Ofelt intensity parameters / Phenomenological intensity parameters depend on both the host lattice and the species of the rare earth ion, where $\lambda = 2, 4, 6$

5.2 Magnetic-dipole Transition

For an electric-dipole transition $\left|l^N SLJ\right\rangle \rightarrow \left|l^N S'L'J'\right\rangle$, the rate of spontaneous radiative decay $A^{MD}_{SLJ\rightarrow S'L'J'}$ is given by:

$$A^{MD}_{SLJ\rightarrow S'L'J'} = \frac{8\pi h\nu^3}{c^3} B^{MD}_{SLJ\rightarrow S'L'J'} \tag{53}$$

The Einstein coefficient:

$$B^{MD}_{SLJ\rightarrow S'L'J'} = \frac{e^2_{SI}}{4hm_e\varepsilon_0\nu} f^{emi}_{MD} \tag{54}$$

where f^{emi}_{MD} is given above.

$$f^{abs}_{MD} = \frac{h\nu}{6m_e c^2}\frac{n}{(2J+1)}\left|\left\langle l^N SLJ|\widehat{L} + g\widehat{S}|l^N SLJ'\right\rangle\right|^2 \tag{55}$$

Therefore,

$$A^{MD}_{SLJ\rightarrow S'L'J'} = \frac{8\pi h\nu^3}{c^3} \times \frac{e^2_{SI}}{4hm_e\varepsilon_0\nu} \times \frac{h\nu}{6m_e c^2}\frac{n}{(2J+1)}\left|\left\langle l^N SLJ|\widehat{L} + g\widehat{S}|l^N SLJ'\right\rangle\right|^2 \tag{56}$$

$\Rightarrow$

$$A^{MD}_{SLJ\rightarrow S'L'J'} = \frac{\pi h e^2_{SI}}{3\varepsilon_0 c^5 m_e^2}\frac{\nu^3}{(2J+1)} n^3 \left|\left\langle l^N SLJ|\widehat{L} + g\widehat{S}|l^N SLJ'\right\rangle\right|^2 \tag{57}$$

5.2.1 Comparison with Emory's Model

Original paper: [49].

$$A^{\mathrm{MD}}_{ij} = \frac{64\pi^4\widetilde{\nu}^3}{3h(2J+1)} n^3 S^{\mathrm{MD}}_{ij} \tag{58}$$

where:

- $S^{\mathrm{MD}}_{ij} = {\mu_{\mathrm{B}}}^2\left|\left\langle [\mathrm{SL}]J_i\|\widehat{L} + 2\widehat{S}\|[\mathrm{SL}]J_j\right\rangle\right|^2$
- $\widetilde{\nu}$ ($\mathrm{cm^{-1}}$): Energy of the transition in wavenumbers
- μ_{B}: Bohr magneton (Gaussian Unit): $\mu_{\mathrm{B}} = \dfrac{e_{cgs}\hbar}{2m_{\mathrm{e}}c}$

$$A_{ij}^{\mathrm{MD}}=\frac{64\pi^4\widetilde{\nu}^3}{3h(2J+1)}n^3(\frac{e_{cgs}\hbar}{2m_{\mathrm{e}}c})^2\left|\left\langle[\mathrm{SL}]J_i\|\widehat{L}+2\widehat{S}\|[\mathrm{SL}]J_j\right\rangle\right|^2 \tag{59}$$

⇒

$$A_{ij}^{\mathrm{MD}}=\frac{64\pi^4\widetilde{\nu}^3}{3h(2J+1)}n^3\frac{e_{cgs}^2h^2}{4\pi^2\times4m_{\mathrm{e}}^2c^2}\left|\left\langle[\mathrm{SL}]J_i\|\widehat{L}+2\widehat{S}\|[\mathrm{SL}]J_j\right\rangle\right|^2 \tag{60}$$

⇒

$$A_{ij}^{\mathrm{MD}}=\frac{4h\pi^2e_{cgs}^2\widetilde{\nu}^3n^3}{3(2J+1)m_{\mathrm{e}}^2c^2}\left|\left\langle[\mathrm{SL}]J_i\|\widehat{L}+2\widehat{S}\|[\mathrm{SL}]J_j\right\rangle\right|^2 \tag{61}$$

Recall $e_{cgs}^2=e_{SI}^2\times\dfrac{1}{4\pi\varepsilon_0}$

⇒

$$A_{ij}^{\mathrm{MD}}=\frac{4h\pi\varepsilon_0e_{cgs}^2\pi(\frac{\nu}{c})^3n^3}{3\varepsilon_0(2J+1)m_{\mathrm{e}}^2c^2}\left|\left\langle[\mathrm{SL}]J_i\|\widehat{L}+2\widehat{S}\|[\mathrm{SL}]J_j\right\rangle\right|^2 \tag{62}$$

⇒

$$A_{ij}^{\mathrm{MD}}=\frac{e_{SI}^2\nu^3h\pi n^3}{3\varepsilon_0(2J+1)m_{\mathrm{e}}^2c^5}\left|\left\langle[\mathrm{SL}]J_i\|\widehat{L}+2\widehat{S}\|[\mathrm{SL}]J_j\right\rangle\right|^2=eq.(41) \tag{63}$$

5.2.2 Comparison with Weber's Model

Original paper: [50].

Magnetic-dipole transitions are parity allowed and subject to selection rules: $\Delta\alpha=\Delta S=\Delta L=0$, and $\Delta J=0,\pm1$(forbidden: $0\rightarrow0$) in the Russel-Saunders limit. The probability for spontaneous emission of magnetic-dipole radiation is given by

$$A_{\mathrm{md}}\left(J;J'\right)=\frac{64\pi^4\nu^3n^3}{(2J+1)3hc^3}\left|\sum_{\alpha SL,\alpha'S'L'}C(\alpha SL)C\left(\alpha'S'L'\right)\left\langle4f^N[\alpha SL]J\|\mathbf{M}\|4f^N\left[\alpha'S'L'\right]J'\right\rangle\right|^2 \tag{64}$$

- $J'=J$

$$\langle f^N\alpha SLJ\|\mathbf{M}\|f^N\alpha'S'L'J\rangle=\delta\left(\alpha,\alpha'\right)\delta\left(S,S'\right)\delta\left(L,L'\right)\beta\left(\frac{2J+1}{4J(J+1)}\right)^{1/2} \tag{65}$$

- $J'=J-1$

$$\langle f^N\alpha SLJ\|\mathbf{M}\|f^N\alpha'S'L'J-1\rangle=\delta\left(\alpha,\alpha'\right)\delta\left(S,S'\right)\delta\left(L,L'\right)\beta\left\{\frac{\left[(S+L+1)^2-J^2\right]\left[J^2-(L-S)^2\right]}{4J}\right\}^{1/2} \tag{66}$$

- $J'=J+1$

$$\langle f^N\alpha SLJ\|\mathbf{M}\|f^N\alpha'S'L'J+1\rangle=\delta\left(\alpha,\alpha'\right)\delta\left(S,S'\right)\delta\left(L,L'\right)\beta\left\{\frac{\left[(S+L+1)^2-(J+1)^2\right]\left[(J+1)^2-(L-S)^2\right]}{4(J+1)}\right\}^{1/2} \tag{67}$$

where:

- $\beta=\dfrac{e\hbar}{2mc}$

- $\hbar = \dfrac{h}{2\pi}$
- h ($\mathrm{g}\cdot\mathrm{cm}^2\cdot\mathrm{s}^{-1}$): Planck constant
- e ($\mathrm{g}^{1/2}\cdot\mathrm{cm}^{3/2}\cdot\mathrm{s}^{-1}$): Elementary charge
- ν (s^{-1}): Transition frequency
- n: Refractive index

5.2.3 Comparison with Norman's Model

Original paper: [52].

The matrix elements for MD transitions are nonzero only if $S = S'$, and $L = L'$. Additional selection rules exist for the total angular momentum J: $J = J', J = J' + 1$, and $J = J' - 1$. The line strength for a magnetic dipole transition can be written as

$$S_{\mathrm{MD}}\left(aJ;bJ'\right) = {\mu_B}^2\left|\left\langle f^n[SL]J\|\widehat{L}+2\widehat{S}\|f^n\left[S'L'\right]J'\right\rangle\right|^2 \tag{68}$$

where $\mu_B = \dfrac{\hbar}{2mc}$. For a given S, L and J of the initial state, the matrix elements in L-S coupling are easily calculated from relations derived from angular momentum considerations. In the L-S coupling scheme the matrix elements for the angular momentum operator $\widehat{L}$ and the spin operator $\widehat{S}$ are:

$$\left\langle f^nSLJ\|\widehat{L}\|f^nS'L'J'\right\rangle = (-1)^{S+L+1+J}\left\{\begin{array}{ccc} S & L & J \\ 1 & J' & L \end{array}\right\}\times\sqrt{L(L+1)(L+2)(2J+1)\left(2J'+1\right)} \tag{69}$$

$$\left\langle f^nSLJ\|\widehat{S}\|f^nS'L'J'\right\rangle = (-1)^{S+L+1+J'}\left\{\begin{array}{ccc} S & L & J \\ J' & 1 & S \end{array}\right\}\times\sqrt{S(S+1)(S+2)(2J+1)\left(2J'+1\right)} \tag{70}$$

Expansion of the 6j symbols and combining above equations together leads to the following equations for the MD matrix elements:

$$\left\langle f^nSLJ\|\widehat{L}+2\widehat{S}\|f^nS'L'J\right\rangle = \left[\frac{2J+1}{4J(J+1)}\right]^{1/2}\left[S(S+1)-L(L+1)+3J(J+1)\right] \tag{71}$$

$$\left\langle f^nSLJ\|\widehat{L}+2\widehat{S}\|f^nS'L'J-1\right\rangle = \left\{\left[(S+L+1)^2-J^2\right]\left[\frac{J^2-(L-S)^2}{4J}\right]\right\}^{1/2} \tag{72}$$

$$\left\langle f^nSLJ\|\widehat{L}+2\widehat{S}\|f^nS'L'J+1\right\rangle = \left\{\left[(S+L+1)^2-(J+1)^2\right]\left[\frac{(J+1)^2-(L-S)^2}{4(J+1)}\right]\right\}^{1/2} \tag{73}$$

5.3 Lifetime of Excited States

The total spontaneous radiative decay rate for a transition $\left|l^NSLJ\right\rangle \rightarrow \left|l^NS'L'J'\right\rangle$ is then given by:

$$A_{SLJ\rightarrow S'L'J'} = A^{ED}_{SLJ\rightarrow S'L'J'} + A^{MD}_{SLJ\rightarrow S'L'J'} \tag{74}$$

In most cases, an excited state $\left|l^NSLJ\right\rangle$ can decay to several lower energy final states $\left|l^NS'L'J'\right\rangle$, and the total radiative decay rate of $\left|l^NSLJ\right\rangle$ is simply the sum of the respective radiative rates. Therefore, the lifetime of the excited state $\left|l^NSLJ\right\rangle$ is given by(consider radiative emission):

$$\tau^{rad}_{SLJ} = \frac{1}{\sum_{S'L'J'}\left(A^{ED}_{SLJ\rightarrow S'L'J'}+A^{MD}_{SLJ\rightarrow S'L'J'}\right)} \tag{75}$$

It is important to note that Eq.(75) only captures radiative contributions to the decay of $\left|l^N SLJ\right\rangle$. There can be additional non-radiative decay mechanisms such as multi-phonon relaxation(MPR) and a variety of energy-transfer processes like cross-relaxation, up-conversion, and energy migration, etc (Section 6.4). The combined rate of these non-radiative decay processes adds to the radiative decay and gives an overall shorter lifetime than the purely radiative lifetime calculated above.

5.4 Branch Ratios

Another characteristic of $\left|l^N SLJ\right\rangle$ excited multiplet is the so-called branching ratio. It is the relative contribution of one $\left|l^N SLJ\right\rangle \rightarrow \left|l^N S'L'J'\right\rangle$ transition to the total radiative decay rate of the $\left|l^N SLJ\right\rangle$ excited multiplet, i.e.

$$\beta_{SLJ\rightarrow S'L'J'} = \frac{A^{ED}_{SLJ\rightarrow S'L'J'} + A^{MD}_{SLJ\rightarrow S'L'J'}}{\sum_{S'L'J'}\left(A^{ED}_{SLJ\rightarrow S'L'J'} + A^{MD}_{SLJ\rightarrow S'L'J'}\right)} \tag{76}$$

The branching ratio is directly accessible in an experiment via the relative intensities of the various emissions from a $\left|l^N SLJ\right\rangle$ excited state in a photo luminescence spectrum. [53][54]

5.5 Multi-phonon Relaxation process(MPR)

From [Emory, JPC, 2012], the rate of multiphonon relaxation, $W^{\mathrm{NR}}_{i,i-1}$, between adjacent levels, can be determined using Van Dijk's modified Energy Gap Law: [55]

$$W^{\mathrm{NR}}_{i,i-1} = W^0_{\mathrm{MPR}} \exp\left[-\alpha\left(\Delta E - 2h\omega_{\max}\right)\right] \tag{77}$$

- ΔE (cm^{-1}): Energy gap to the next lower multiplet
- $h\omega_{\max}$ (cm^{-1}): The highest phonon energy of the host materials
- W^0_{MPR} (s^{-1}): Zero-phonon relaxation rate
- α (cm): MPR rate constant

6 Case study: $\mathrm{Yb}^{3+}, \mathrm{Tm}^{3+}, \mathrm{Er}^{3+}$ in NaYF_4

To accelerate the simulation, we manually truncated some energy levels above a threshhold level of Tm^{3+} and Er^{3+}. Below such threshold, we calculated all allowed transitions including ED, MD, MPR, ET. All of these Russell Saunders notations ($^{2S+1}\mathrm{L_J}$) and energies E_i are cited from [56], and [Emory, JPC, 2012], respectively.

We consider the following energy levels of Tm^{3+}:

Tm^{3+}	Notation	Values (cm^{-1})
$^1\mathrm{D}_2$	E_7	28028
$^1\mathrm{G}_4$	E_6	21352
$^3\mathrm{F}_2$	E_5	15180
$^3\mathrm{F}_3$	E_4	14598
$^3\mathrm{H}_4$	E_3	12735
$^3\mathrm{H}_5$	E_2	8396
$^3\mathrm{F}_4$	E_1	5828
$^3\mathrm{H}_6$	E_0	153

We consider the following energy levels of Er^{3+}:

Er^{3+}	Notation	Values (cm^{-1})
$^2P_{3/2}$	E_{15}	31414
$^2G(1)_{7/2}$	E_{14}	27825
$^2K_{15/2}$	E_{13}	27584
$^4G_{9/2}$	E_{12}	27319
$^4G_{11/2}$	E_{11}	26376
$^2G(1)_{9/2}$	E_{10}	24475
$^4F_{3/2}$	E_9	22677
$^4F_{5/2}$	E_8	22282
$^4F_{7/2}$	E_7	20497
$^2H_{11/2}$	E_6	19246
$^4S_{3/2}$	E_5	18448
$^4F_{9/2}$	E_4	15306
$^4I_{9/2}$	E_3	12553
$^4I_{11/2}$	E_2	10230
$^4I_{13/2}$	E_1	6632
$^4I_{15/2}$	E_0	0

6.1 Pure Wavefunction Approximation

The ED and MD transition intensity calculation builds on RME of the $\widehat{U}^{(k)}$ and $\widehat{L}+g\widehat{S}$ tensor operators, respectively, which in turn directly depend on the wavefunctions(under intermediate coupling scheme) of the involved electronic configurations: $^{2S+1}L_J$. Therefore, the proper application of the J-O theory first, requires the calculation of high-quality wavefunctions for the material system($NaYF_4$) which then serve as the basis for the intensity calculation.

It is challenging that in addition to the a set of Slater integrals $F_{(2)}, F_{(4)}, F_{(6)}$, relevant coefficients e_k, and the spin–orbit coupling parameter ζ in a given material $NaYF_4$ that are required to the construction of matrix elements of $\widehat{H}_e$ and $\widehat{H}_{so}$. Additionally, the matrix of total Hamiltonian operator $\widehat{H}=\widehat{H}_e+\widehat{H}_{so}$ has off-diagonal elements, that arise from mixing of different states with the same J by spin-orbit coupling as well as from mixing of states with the same S and L by electrostatic interaction. Square symmetric matrix diagonalization algorithms such as the **Jacobi method** can be employed to solve such tedious computational task, to obtain both the energies E_i as the corresponding eigenvalues and the coefficients c_i of the intermediate coupling wavefunctions $\left|4f^N SLJ\right\rangle$.

However, we found that both [Emory, JPC, 2012] and [M.J. Weber, PR, 1967], for both ED and MD transition intensity calculation, they used the pure wave function instead of the intermediate-coupling wavefunction for each energy level. Also, from the Table-2([56]), wave functions of each energy level $\left|4f^N SLJ\right\rangle$ are mixtures of wave functions of other energy levels with the same J (J-mixing), but their main component is still themselves. We can also find the similar reports in above Table I, Weber's paper. As a result, we decide firstly use the pure wave function for ED and MD transition intensity calculation in our case.

6.2 Basic Constants

6.2.1 Judd-Ofelt Intensity Parameters Ω_λ

Ω_λ (cm^2) depends on both the host lattice and the species of the rare earth ion. We obtain Ω_λ from SI of [Emory, JPC, 2012]. We assume Ω_λ in whether $NaYF_4$ or $NaYbF_4$ are equal.

Lanthanide ion	Ω_2	Ω_4	Ω_6
Er^{3+}	$2.11\times10^{-20}\,cm^2$	$1.37\times10^{-20}\,cm^2$	$1.22\times10^{-20}\,cm^2$
Tm^{3+}	$2.04\times10^{-20}\,cm^2$	$2.01\times10^{-20}\,cm^2$	$1.44\times10^{-20}\,cm^2$

6.2.2 Refractive Index n

Refractive index $n=1.5$ of $NaYF_4$ from SI of [Emory, JPC, 2012], which we assume n is a constant. More detailed information about Sellmeier equation can be found in Section (4.5).

6.2.3 Local Field Correction χ

Emory takes the $n \times \chi_{ED}^{abs}$ as the local field correction, where χ_{ED}^{abs} is the local-field correction for an ED-induced absorption. A detailed investigation can be found in Section (4.4). The Local field correction χ used in our calculation given below:

$$\chi = \frac{n\left(n^2+2\right)^2}{9} \tag{78}$$

6.3 Radiative Emission Intensity Calculation

6.3.1 ED Radiative Rmission [Colab]

- Calculated ED transition rates of Tm^{3+} (SI: Table.5)
- Calculated ED transition rates of Er^{3+} (SI: Table.6, Table.7)

6.3.2 MD Radiative Emission [Colab]

- Calculated MD transition rates of Tm^{3+} (SI: Table.8)
- Calculated MD transition rates of Er^{3+} (SI: Table.9, Table.10)

6.4 Non-radiative Emission Intensity Calculation

From [Emory, JPC, 2012], the rate of multiphonon relaxation, $W_{i,i-1}^{\mathrm{NR}}$, between adjacent levels, can be determined using Van Dijk's modified Energy Gap Law: [58]

$$W_{i,i-1}^{\mathrm{NR}} = W_{\mathrm{MPR}}^{0} \exp\left[-\alpha\left(\Delta E - 2h\omega_{\max}\right)\right] \tag{79}$$

- ΔE (cm^{-1}): Energy gap to the next lower manifold
- $h\omega_{\max}$ (cm^{-1}): The highest phonon energy of the host materials
- W_{MPR}^{0} (s^{-1}): Zero-phonon relaxation rate(s^{-1})
- α (cm): MPR rate constant

We use the following values from SI of [Emory, JPC, 2012]

Constants	$h\omega_{\max}$	W_{MPR}^{0}	α
Values	450	2×10^{7}	3.5×10^{-3}

6.4.1 Multi-phonon Relaxation(MPR) [Colab]

Instead of merely caring about adjacent levels, we introduce the gap threshold: 3000 (cm^{-1}) [M.J. Weber, PR, 1967], so we consider any two pairs that the net energy gap is smaller than 3000 (cm^{-1}).

- Calculated MPR rate of Tm^{3+} (SI: Table.11)
- Calculated MPR rate of Er^{3+} (SI: Table.12, Table.13)

6.4.2 Phonon-assisted Energy Transfer(PET) [Colab]

For an isolated donor-acceptor pair, the orientation-averaged rate of dipole-dipole energy transfer, $A^{\mathrm{ET}}_{ij,kl}$ with donor transition $i \to j$ and acceptor transition $k \to l$, can be described as a function of the interionic distance R, and the electric-dipole line strengths of the acceptor(S^{ED}_{ij}) and donor(S^{ED}_{kl}) transitions as determined by J − O theory: [59]

The essential part of ET rate is:

$$C_{\mathrm{ij,kl}^{RET}} = \frac{1}{R^6}\left[\frac{8\pi^2 e^4 s_{ij,kl}}{3h^2 c g_i g_k}\right]\left(\frac{n^2+2}{3n}\right)^4 S^{\mathrm{ED}}_{ij} S^{\mathrm{ED}}_{kl} \tag{80}$$

where:

- $S^{\mathrm{ED}}_{ij} = \sum_{\lambda=2,4,6} \Omega_\lambda \left|\left\langle SLJ \left\| U^{(\lambda)} \right\| SLJ' \right\rangle\right|^2$: Electric-dipole line strengths
- $s_{ij,kl}$ (cm): The overlap integral between the normalized donor emission spectrum ($i \to j$) and acceptor absorption spectrum ($k \to l$)
- g_i/g_k: Degeneracy of initial level of donor/acceptor, which is the $(2J+1)$ number of states in manifold i/k
- R (cm): interionic distance

Since it is not easy to evaluate the overlap integral of donor transition $i \to j$ and acceptor transition $k \to l$, so we temporarily assume the overlap integral of $Yb^{3+} - Tm^{3+}$ is a constant approximately, calculated from [Emory, JPC, 2012]: $s = 0.00014$ (cm) [Colab]

However, the fact is that most energy transfer processes are not resonant, so the phonon must be involved to conserve energy, and we should introduce a **correction factor** to modify the resonant energy transfer formula. Miyakawa and Dexter modified the expression for resonant energy transfer(RET) rates with an exponential dependence related to the Energy Gap Law. We can then write the phonon-assisted energy transfer microparameter as: [60]

$$C^{\mathrm{PET}}_{\mathrm{ij,kl}} = C^{RET}_{\mathrm{ij,kl}} \exp\left[-\beta_{\mathrm{MPR}} \Delta E\right] \tag{81}$$

where:

- $h\omega = 450$ (cm^{-1}): The maximum phonon energy in host material
- $\gamma = \dfrac{\ln(2)}{h\omega}$
- $\alpha = 3.5 \times 10^{-3}$ (cm)
- $\beta_{\mathrm{MPR}} = \alpha - \gamma = 2 \times 10^{-3}$ (cm): A material-dependent constant related to the MPR constant α
- ΔE: The net energy difference between the donor transition: $i \to j$ and acceptor transitions $k \to l$.

Therefore, the non-resonant energy transfer rate between a pair of ions: Yb^{3+}-Tm^{3+}, and Yb^{3+}-Er^{3+} can be expressed as:

$$A_{ij,kl} = \frac{1}{R^6}\left[\frac{8\pi^2 e^4_{cgs} s_0}{3h^2 c g_i g_k}\left(\frac{n^2+2}{3n}\right)^4 S^{\mathrm{ED}}_{ij} S^{\mathrm{ED}}_{kl}\right] \times \exp(-\beta_{\mathrm{MPR}} \Delta E) \tag{82}$$

Please note that the overlap integral of Yb^{3+}-Yb^{3+} : $s' = 0.001$cm [50], and the energy transfer between Yb^{3+} ions can be treated as resonant energy transfer, so there is no need to introduce the correction factor for Yb^{3+}-Yb^{3+} calculation.

6.4.3 ET Energy Matching Condition

Based on the phonon-assisted energy transfer(PET) analysis above, we are ready to evaluate all resonant and non-resonant energy transfer processes, which can be further divided into three groups:

- Energy migration process(Resonant ET): $Yb^{3+} \leftrightarrow Yb^{3+}$
- Up-conversion process(Non-resonant ET): $Yb^{3+} \rightarrow Tm^{3+}, Yb^{3+} \rightarrow Er^{3+}$
- Cross-relaxation process(Non-resonant ET): $Tm^{3+} \leftrightarrow Tm^{3+}, Er^{3+} \leftrightarrow Er^{3+}$

In reality, there are numerous possible situations in which energy can be transferred between any two ions, which makes the energy network extremely complex. All possible energy transfer processes:

$$\mathrm{ET} = \left[\sum_{donors} i \rightarrow j\right] \times \left[\sum_{acceptors} k \rightarrow l\right] \tag{83}$$

However, a paper [59] claims that there exists a so-called **energy-matching condition**, which means the net energy difference ΔE of the selected two pairs: $E_{i\rightarrow j}$ and $E_{k\rightarrow l}$ are less than the maximum phonon energy $\hbar\omega$, i.e. $\Delta E = |\Delta E_{i\rightarrow j} - \Delta E_{k\rightarrow l}| \leq \hbar\omega$.

However, from [Dayong Jin, JPC, 2012], whether the the up-conversion processes or cross-relaxation process between Yb^{3+} and Tm^{3+}, don't meet the energy-matching condition. See more details below.

A. $Yb_i \rightarrow Yb_j$:

(A.1). Resonant energy transfer process c_0:

- $\left|{}^2F_{5/2}(Yb_i), {}^2F_{7/2}(Yb_j)\right\rangle \rightarrow \left|{}^2F_{7/2}(Yb_i), {}^2F_{5/2}(Yb_j)\right\rangle$
- $\left|{}^2F_{5/2}(Yb_i)\right\rangle \rightarrow \left|{}^2F_{7/2}(Yb_i)\right\rangle$: $\Delta E_1 = 10204\ \mathrm{cm}^{-1}$
- $\left|{}^2F_{7/2}(Yb_j)\right\rangle \rightarrow \left|{}^2F_{5/2}(Yb_j)\right\rangle$: $\Delta E_2 = 10204\ \mathrm{cm}^{-1}$
- $\Delta E = |\Delta E_1 - \Delta E_2| = 0\ \mathrm{cm}^{-1}$ (Resonant ET)

B. $Yb_i \rightarrow Tm_j$

(B.1). Up-conversion process: c_1:

- $\left|{}^2F_{5/2}(Yb_i), {}^3H_6(Tm_j)\right\rangle \rightarrow \left|{}^2F_{7/2}(Yb_i), {}^3H_5(Tm_j)\right\rangle$
- $\left|{}^2F_{5/2}(Yb_i)\right\rangle \rightarrow \left|{}^2F_{7/2}(Yb_i)\right\rangle$: $\Delta E_1 = 10204\ \mathrm{cm}^{-1}$
- $\left|{}^3H_6(Tm_j)\right\rangle \rightarrow \left|{}^3H_5(Tm_j)\right\rangle$: $\Delta E_2 = 8243\ \mathrm{cm}^{-1}$
- $\Delta E = |\Delta E_1 - \Delta E_2| = 1961\ \mathrm{cm}^{-1}$

(B.2). Up-conversion process: c_2:

- $\left|{}^2F_{5/2}(Yb_i), {}^3F_4(Tm_j)\right\rangle \rightarrow \left|{}^2F_{7/2}(Yb_i), {}^3F_3(Tm_j)\right\rangle$
- $\left|{}^2F_{5/2}(Yb_i)\right\rangle \rightarrow \left|{}^2F_{7/2}(Yb_i)\right\rangle$: $\Delta E_1 = 10204\ \mathrm{cm}^{-1}$
- $\left|{}^3F_4(Tm_j)\right\rangle \rightarrow \left|{}^3F_3(Tm_j)\right\rangle$: $\Delta E_2 = 8770\ \mathrm{cm}^{-1}$
- $\Delta E = |\Delta E_1 - \Delta E_2| = 1434\ \mathrm{cm}^{-1}$

(B.3). Up-conversion process: c_3:

- $\left|{}^2F_{5/2}(Yb_i), {}^3H_4(Tm_j)\right\rangle \rightarrow \left|{}^2F_{7/2}(Yb_i), {}^1G_4(Tm_j)\right\rangle$
- $\left|{}^2F_{5/2}(Yb_i)\right\rangle \rightarrow \left|{}^2F_{7/2}(Yb_i)\right\rangle$: $\Delta E_1 = 10204\ \mathrm{cm}^{-1}$
- $\left|{}^3H_4(Tm_j)\right\rangle \rightarrow \left|{}^1G_4(Tm_j)\right\rangle$: $\Delta E_2 = 8617\ \mathrm{cm}^{-1}$
- $\Delta E = |\Delta E_1 - \Delta E_2| = 1587\ \mathrm{cm}^{-1}$

(B.4). Up-conversion process: c_4:

- $\left|^2\mathrm{F}_{5/2}(\mathrm{Yb_i}), {}^1\mathrm{G}_4(\mathrm{Tm_j})\right\rangle \rightarrow \left|^2\mathrm{F}_{7/2}(\mathrm{Yb_i}), {}^1\mathrm{D}_2(\mathrm{Tm_j})\right\rangle$
- $\left|^2\mathrm{F}_{5/2}(\mathrm{Yb_i})\right\rangle \rightarrow \left|^2\mathrm{F}_{7/2}(\mathrm{Yb_i})\right\rangle$: $\Delta E_1 = 10204\ \mathrm{cm}^{-1}$
- $\left|^1\mathrm{G}_4(\mathrm{Tm_j})\right\rangle \rightarrow \left|^1\mathrm{D}_2(\mathrm{Tm_j})\right\rangle$: $\Delta E_2 = 6676\ \mathrm{cm}^{-1}$
- $\Delta E = |\Delta E_1 - \Delta E_2| = 3528\ \mathrm{cm}^{-1}$

C. $\mathrm{Tm_i} \rightarrow \mathrm{Tm_j}$
(C.1). Cross-relaxation k_{31}:

- $\left|^3\mathrm{H}_4(\mathrm{Tm_i}), {}^3\mathrm{H}_6(\mathrm{Tm_j})\right\rangle \rightarrow \left|^3\mathrm{F}_4(\mathrm{Tm_i}), {}^3\mathrm{F}_4(\mathrm{Tm_j})\right\rangle$
- $\left|^3\mathrm{H}_4(\mathrm{Tm_i})\right\rangle \rightarrow \left|^3\mathrm{F}_4(\mathrm{Tm_i})\right\rangle$: $\Delta E_1 = 6907\ \mathrm{cm}^{-1}$
- $\left|^3\mathrm{H}_6(\mathrm{Tm_j})\right\rangle \rightarrow \left|^3\mathrm{F}_4(\mathrm{Tm_j})\right\rangle$: $\Delta E_2 = 5675\ \mathrm{cm}^{-1}$
- $\Delta E = |\Delta E_1 - \Delta E_2| = 1232\ \mathrm{cm}^{-1}$

(C.2). Cross-relaxation k_{41}:

- $\left|^1\mathrm{G}_4(\mathrm{Tm_i}), {}^3\mathrm{H}_6(\mathrm{Tm_j})\right\rangle \rightarrow \left|^3\mathrm{H}_5(\mathrm{Tm_i}), {}^3\mathrm{H}_4(\mathrm{Tm_j})\right\rangle$
- $\left|^1\mathrm{G}_4(\mathrm{Tm_i})\right\rangle \rightarrow \left|^3\mathrm{H}_5(\mathrm{Tm_i})\right\rangle$: $\Delta E_1 = 12956\ \mathrm{cm}^{-1}$
- $\left|^3\mathrm{H}_6(\mathrm{Tm_j})\right\rangle \rightarrow \left|^3\mathrm{H}_4(\mathrm{Tm_j})\right\rangle$: $\Delta E_2 = 12582\ \mathrm{cm}^{-1}$
- $\Delta E = |\Delta E_1 - \Delta E_2| = 374\ \mathrm{cm}^{-1}$

(C.3). Cross-relaxation k_{51}:

- $\left|^1\mathrm{D}_2(\mathrm{Tm_i}), {}^3\mathrm{H}_6(\mathrm{Tm_j})\right\rangle \rightarrow \left|^3\mathrm{F}_2(\mathrm{Tm_i}), {}^3\mathrm{H}_4(\mathrm{Tm_j})\right\rangle$
- $\left|^1\mathrm{D}_2(\mathrm{Tm_i})\right\rangle \rightarrow \left|^3\mathrm{F}_2(\mathrm{Tm_i})\right\rangle$: $\Delta E_1 = 12848\ \mathrm{cm}^{-1}$
- $\left|^3\mathrm{H}_6(\mathrm{Tm_j})\right\rangle \rightarrow \left|^3\mathrm{H}_4(\mathrm{Tm_j})\right\rangle$: $\Delta E_2 = 12582\ \mathrm{cm}^{-1}$
- $\Delta E = |\Delta E_1 - \Delta E_2| = 266\ \mathrm{cm}^{-1}$

According to **energy-matching condition**, we find 15 cross-relaxation processes between Tm^{3+}-Tm^{3+} while there are no up-conversion processes allowed between Yb^{3+}-Tm^{3+}. Likewise, there are totally 282 cross-relaxation processes between Er^{3+}-Er^{3+} while there are only three up-conversion processes allowed between Yb^{3+}-Er^{3+}. Therefore, in order to get the Monte Carlo model worked firstly, we simplified the energy transfer processes, in which we only consider widely reported up-conversion processes and cross-relaxation processes.

Based on above analysis, here are our calculated RET/PET rates:

- Calculated RET of $Yb^{3+} \leftrightarrow Yb^{3+}$ (SI: Table.14)
- Calculated Up-conversion rate(PET) of $Yb^{3+} \rightarrow Tm^{3+}$ (SI: Table.15)
- Calculated Cross-relaxation rate(PET) of $Tm^{3+} \leftrightarrow Tm^{3+}$ (SI: Table.16)

6.5 Monte Carlo Simulation [Colab]

Recall that this research endeavors to advance the understanding of energy transfer dynamics within UCNPs by developing and refining a Monte-Carlo model. Grounded in an extensive theoretical framework and calculated transition rates so far, the various mechanisms involved in energy redistribution are examined, including resonant energy transfer process(RET), phonon-assisted energy transfer process(PET)(up-conversion, cross-relaxation), electric dipole (ED) and magnetic dipole (MD) radiative emissions, and multi-phonon relaxation.

The Monte Carlo model, which is currently in the refinement stage to ensure its predictions accurately mirror experimental findings. It integrates several critical components and reasonable assumption to simulate the complex transition behaviors of UCNPs with high fidelity:

- Ion spatial distribution

The model conceptualizes nanoparticles as hexagonal crystal structures(β-phase), where Yb^{3+} or Tm^{3+} ions are randomly distributed. This approach not only captures the inherent spatial relationships characteristic of hexagonal crystallinity but also facilitates a realistic representation of ion dispersion within the nanoparticle matrix.

- Critical interacting distance R_0

Acknowledging the inverse sixth power dependence of the energy transfer rate on the inter-ionic distance (R), the model introduces a critical interaction distance $R_0 = 1$ nm. This pragmatic adjustment allows for the efficient simulation of ion interactions by limiting the consideration of effective neighbors to those within this defined radius, thus optimizing computational resources without compromising the model's integrity.

- High energy levels truncation

Our simulations reveal that very few population inhabit in higher energy levels that have negligible contribution to the desired emission, and we have decided to truncate higher energy levels so that computational complexity can be also reduced. Meanwhile manually restricting the transition options for different ions at different levels.

- Probabilistic process modeling

The simulation timescale operates over $T = 1$ s, segmented into nanosecond increments $\Delta t = 1$ us yielding a comprehensive resolution of 1×10^6 steps. Each step assesses the state of excited sensitizer Yb^{3+} and emitter Tm^{3+} and their immediate neighbors within R_0, determining the subsequent mutual competitive energy transfer events, through a probabilistic comparison between a generated random number p_i, and established all transition rates $W = \{\text{ED} + \text{MD}, \text{Up} - \text{conversion}, \text{Cross} - \text{relaxation}, \text{Stay}\}$.

- Emission transition selection

A pivotal aspect of the simulation involves tracking and quantifying transition events over time: 10^6 steps with $\Delta t = 1$ us, $T = 1$ s, and across specific wavelength bands, i.e. Blue ($\lambda \leq 510$ nm), Green ($510 \leq \lambda \leq 705$ nm), and near-infrared (NIR) ($705 \leq \lambda \leq 850$ nm). The objective is to calculate the emission intensity in photons per second (pps), which serves as a standard for model validation against experimental observations.

6.5.1 Model Outputs

All simulation outputs and interacting figures can be found in Colab.

- Saturation curves [Colab]
- Population evoluations [Colab]

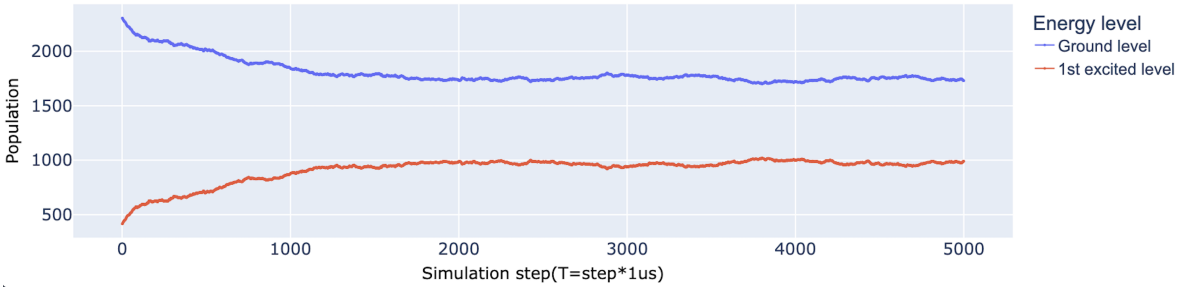

Figure 3: Simulated population of Yb^{3+} of two energy levels

Figure 4: Simulated population of Tm^{3+} of eight energy levels

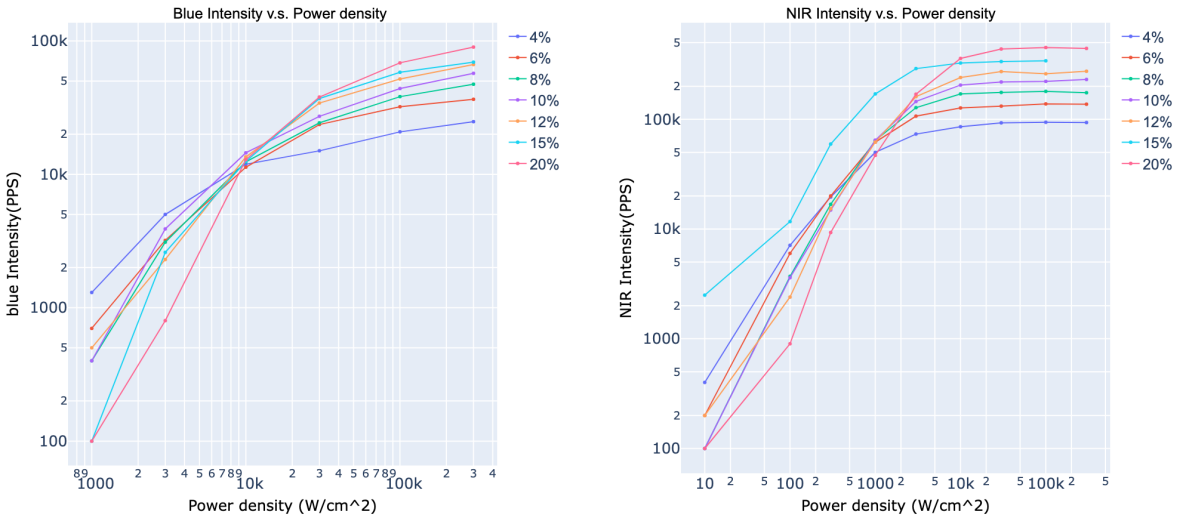

Figure 5: Power-dependent Emission intensities of single nanoparticle over various concentrations

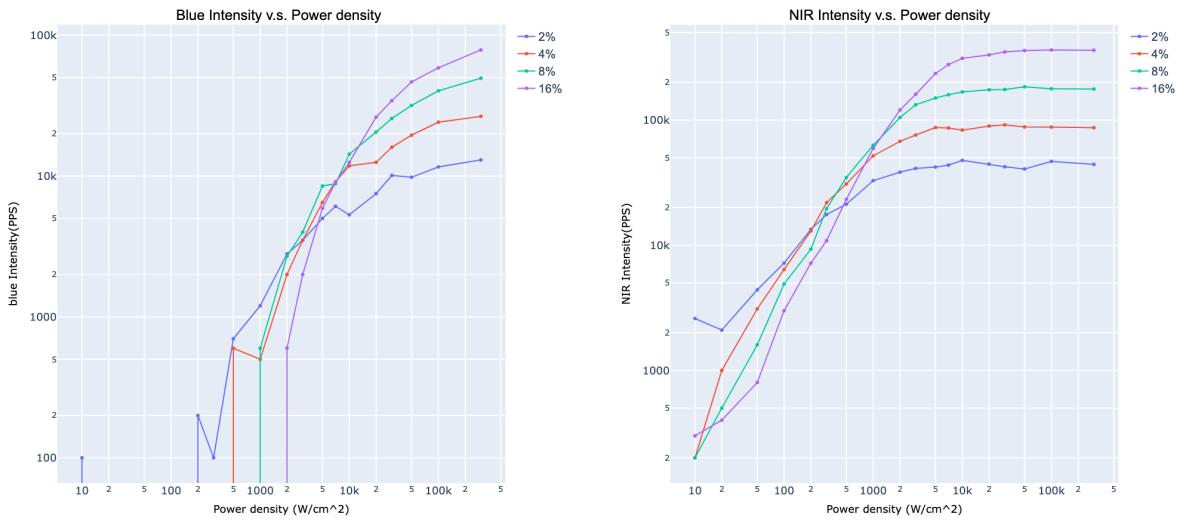

Figure 6: Power-dependent Emission intensities of single nanoparticle over various concentrations(Intensity Inversion)

6.6 Conclusion

6.6.1 What I Have Achieved

- Theoretical framework: Initiated with an in-depth investigation into the electronic structure of lanthanide ions by leveraging the Judd-Ofelt theory.
- Literature review: Conducted a comprehensive literature review to identify and derive essential formulations for calculating energy transfer rates within UCNPs, encompassing ED, MD, MPR, RET and PET.
- Parameter acquisition: Identified critical physical constants such as Judd-Ofelt intensity parameters (Ω_λ), the refractive index (n), phonon-related constants (α, β) specific to the host materials and dopant ions (Yb^{3+}, Tm^{3+}, Er^{3+})
- Monte Carlo model: Developed and implemented a Monte Carlo model for the Yb^{3+}-Tm^{3+} system, incorporating reasonable assumptions including: higher levels truncation, critical interacting distance R_0, and simulation timestep Δt, etc.

6.6.2 Simulation Results

- Saturation curves and concentration-dependent relations: Reproduce part of the saturation curves and concentration-dependent relations, including the observation of 'Intensity Inversion' phenomena.
- Steady-State Population: Produce steady-state population results for each energy level of both sensitizers and emitters, consistent with results from another common numerical simulation method (ODE).

7 Summary & Outlook

7.1 Model Evaluation

7.1.1 Advantages

- We start from a very intuitive point view, consider each ion's energy state and behavior, and the stepwise energy transition among these states, containing decay rates and energy transfer rates without much artificial assumptions, so it is what it is.

- We generated the crystal structure model with randomly embedded ions into these lattice site, which realistically imitates the chemical synthesis process. Hence we have the reason to believe these ions's interaction and final output over a certain period of time can properly reflect what's going on in real system.
- From a very fundamental physical perspective, the selection rule that governs the ion energy state changing results form the symmetry breaking, which means ions at different area of the inorganic crystal $NaYF_4$ should have different local site symmetry. Although it has been reported that no detailed knowledge on such local site information for each doped ion becomes necessary in the evaluation of the emission intensity from the whole, but our model is highly scalable that can further enable us to introduce more detailed information of such lanthanide-doped nanocrystal, a promising point is the rational design of selection rules to manipulate the microscopic transition probability.

7.1.2 Defects

- The basic constants that used in all kinds of formulations are not strictly perfect, but from secondary sources. Differences in the materials themselves, the actual energy levels of the ions in the crystal, the measurement methods of physical constants, etc. will all bring inevitable errors.
- In order to accelerate the simulation process, we truncate some higher energy levels and manually limit interacting range of each ion, which may not capture full properties of real UCNPs system, although we should and we can embrace all transition rates for each single ion or any pair ions.
- We are still using reported radiative and non-radiative processes, possibly overlooking hidden processes that are not easily discovered through the MC model.

7.2 Potential Improvements

- Refining the accuracy of basic constants and parameters by sourcing direct measurements from analogous materials.
- Expanding the model to include all possible transition rates and interactions without simplifications, thus closely mimicking the actual UCNPs dynamics.
- Investigating and incorporating potential hidden processes into the model to provide a more comprehensive understanding of UCNPs luminescence behavior.
- Parallel computing and high-performance simulation frameworks. Explore the use of parallel computing techniques and the development of high-performance computational frameworks to significantly reduce simulation times, enabling the investigation of mixture and more complex UCNPs systems.
- Nano-Engineering for enhanced upconversion Efficiency. Combine insights from other materials (e.g. plasmonic nanoparticles, quantum dots, etc) to explore the effects of doping concentration, particle size, core-shell structure, and surface modification on upconversion efficiency.

This research report delves into the 4f-electron spectroscopic properties of Yb^{3+}, Tm^{3+}, and Er^{3+} in inorganic nanocrystal β-$NaYF_4$, leveraging the Judd-Ofelt(J-O) theory to investigate energy transfer mechanism of up-conversion nanoparticles(UCNPs). Through an extensive literature and detailed derivation processes, we have identified essential formulations for calculating energy transfer rates including these following four dominent processes: electric-dipole (ED)radiative emission, magnetic-dipole (MD) radiative emission, phonon-assisted non-resonant energy transfer rate(PET), and multi-phonon relaxation rates(MPR). Utilizing these formulations, transition rates for Yb^{3+}-Tm^{3+} and Yb^{3+}-Er^{3+} systems were calculated and verified, laying the groundwork for a Monte Carlo (MC) simulation that successfully partially reproduced saturation curves, concentration-dependent relations, and the intensity inversion phenomenon. Based on all above calculation with J-O theory, the MC model crafted with reasonable assumptions and closely reflecting chemical synthesis through its simulated crystal structure and ions distribution, stands out for its intuitive approach to ion interactions and scalability. Despite its innovation, the model faces limitations due to the non-ideal constants, simplified

core-shell structure, and oversight of potential hidden processes. Future efforts will focus on refining these aspects to develop a more accurate and comprehensive computational framework to advance the development of UCNPs with distinguishable emission, enhanced energy transfer efficiency, and sufficient stable luminescent intensity, to further facilitate the multi-color, long-term single particle tracking for bio-molecule behaviors investigation.

8 Supplementary Information

8.1 Reproduction of Others Parameters

8.1.1 Emory, JPC, 2012 [Colab]

(1). Judd-Ofelt intensity parameters $\Omega_\lambda(cm^2)$ of Er^{3+} and Tm^{3+} in $NaYF_4$.

Lanthanide ion	Ω_2	Ω_4	Ω_6
Er^{3+}	$2.11 \times 10^{-20}\,cm^2$	$1.37 \times 10^{-20}\,cm^2$	$1.22 \times 10^{-20}\,cm^2$
Tm^{3+}	$2.04 \times 10^{-20}\,cm^2$	$2.01 \times 10^{-20}\,cm^2$	$1.44 \times 10^{-20}\,cm^2$

Table 1: Emory: $\Omega_\lambda(cm^2)$ of Er^{3+},Tm^{3+} in $NaYF_4$

(2). Squared RME for $J \to J'$ ED transition.

Er^{3+} or Tm^{3+}	$^4F_{9/2} \to {}^4I_{15/2}$	$^4S_{3/2} \to {}^4I_{15/2}$	$^3F_4 \to {}^3H_6$	$^4I_{13/2} \to {}^4I_{15/2}$
$\lvert U^{(2)}\rvert^2$	0	0	0.527	0.0195
$\lvert U^{(4)}\rvert^2$	0.5354	0	0.718	0.1173
$\lvert U^{(6)}\rvert^2$	0.4619	0.2211	0.228	1.4316

Table 2: Emory: Squared RME for $J \to J'$ ED transition

(3). Refractive index of β-$NaYF_4$ and local field correction: $\chi = \dfrac{n\left(n^2+2\right)^2}{9}$, with $n = 1.5$

- Case-1: Er^{3+}+Tm^{3+} (SI: Section ??)
- Case-2: Er^{3+} alone (SI: Section 20)

8.1.2 Weber, Physical Review, 1967 [Colab]

(1). Judd-Ofelt intensity parameters $\Omega_\lambda(cm^2)$ of Er^{3+} in LaF.

Lanthanide ion	Ω_2	Ω_4	Ω_6
Er^{3+}	$1.08 \times 10^{-20}\,cm^2$	$0.28 \times 10^{-20}\,cm^2$	$0.64 \times 10^{-20}\,cm^2$

Table 3: Weber: $\Omega_\lambda(cm^2)$ of Er^{3+} in LaF

(2). Squared RME for $J \to J'$ ED transition.

(3). Refractive index of LaF and local field correction: $\chi = \dfrac{n\left(n^2+2\right)^2}{9}$ with $n = 2.02$.

- ED-radiative emission parameters (SI: Section ??)
- MD-radiative emission parameters (SI: Section 22, 23)

8.2 Experiments Fitting of Barycenter Energy E_B

Actually, we should have good wavefunctions $\left|4f^N SLJ\right\rangle$ for a system before performing a Judd–Ofelt intensity calculation. The weak interactions of the Ln^{3+} with its surroundings affect both the effective electrostatic and spin–orbit coupling strength to some extent.

Er^{3+}	$^4I_{13/2} \rightarrow {}^4I_{15/2}$	$^4I_{11/2} \rightarrow {}^4I_{15/2}$	$^4I_{11/2} \rightarrow {}^4I_{13/2}$
$\lvert U^{(2)}\rvert^2$	0.0188	0.0259	0.021
$\lvert U^{(4)}\rvert^2$	0.1176	0.0001	0.11
$\lvert U^{(6)}\rvert^2$	1.4617	0.3994	1.04

Table 4: Weber: Squared RME for $J \rightarrow J'$ ED transition

Crystal-field interaction(C-F) cause a partial/complete splitting of each $^{2S+1}L_J$ multiplet into its $2J+1$ components, depending on the Ln^{3+} ion and point symmetry at the Ln^{3+} site. Beyond that, external field like magnetic field or electrical field can also cause the $^{2S+1}L_J$ to be splitted into more sublevels, so the multiplicity is at least $2J+1$. The term 2J+1 describes the degeneracy of the state associated with the quantum number J. It comes from the fact that m_j can take any integer value between $-J$ and $+J$.

2. Barcenter energy E_B

$$E_B\left(^{2S+1}L_J\right) = \frac{1}{2J+1}\sum_i g_i E_i \tag{84}$$

where the sum runs over all crystal-field levels with energies E_i of the $^{2S+1}L_J$ multiplet, and g_i is the crystal-field level degeneracy $\sum_i (g = 2J+1)_i$. Firstly use low-temperature polarized absorption and luminescence spectroscopy to find the energy and degeneracy of each crystal-field level of each $^{2S+1}L_J$ multiplet, then calculating the barycenter energies according to above equation. Note that it is not practical for amorphous systems such as Ln^{3+}-doped glasses and solutions.

Finally, the electrostatic $\left(F_{(2)}, F_{(4)}, F_{(6)}\right)$ and spin-orbit (ζ) parameters can be obtained by fitting calculated E_B^{calc} to a set of experimental E_B^{exp}. Choose to either minimize the absolute root-mean-square (RMS) deviation or the relative RMS deviation(better)

$$\mathrm{RMS}_{abs} = \sqrt{\frac{1}{n-p}\sum_{i=1}^{n}\left(E_i^{\mathrm{exp}} - E_i^{\mathrm{calc}}\right)^2} \tag{85}$$

$$\mathrm{RMS}_{rel} = \sqrt{\frac{1}{n-p}\sum_{i=1}^{n}\left(\frac{E_i^{\mathrm{exp}} - E_i^{\mathrm{calc}}}{E_i^{\mathrm{exp}}}\right)^2} \tag{86}$$

where n is the number of experimental barycenter energies and p is the number of fit parameters (p=4 in this case). Now given set of electrostatic $F_{(2)}, F_{(4)}, F_{(6)}$ for $\widehat{H}_e$ and spin–orbit (ζ) parameters for $\widehat{H}_{so}$, we can obtain the intermediate coupling wavefunction Ψ (3.4). With $\widehat{U}^{(k)}$ and $\widehat{L} + g\widehat{S}$, we can calculate ED and MD oscillator strengths as a function of a set of three $\Omega_{(\lambda)}, \lambda = 2, 4, 6$ Judd–Ofelt intensity parameters. The calculated total oscillator strengths can then be compared to experimental oscillator strengths as part of the procedure for fitting the $\Omega_{(\lambda)}$ parameters.

8.3 Experimental Fitting for Oscillator Strengths f

Tetragonal, hexagonal, and trigonal crystal systems are typically uniaxial, i.e. having an extraordinary axis $\vec{c}$ that is different from the other axes $\vec{a}$. Experimental oscillator strengths are typically determined from absorption spectra(determined from σ and π polarized room-temperature absorption spectra according to $f_{avg} = 2f_\sigma + f_\pi$ [58], and are calculated according to:

$$f_{\mathrm{exp}} = \frac{4\varepsilon_0 m_e c^2}{e^2}\frac{10\ln(10)}{N_A}\int \varepsilon(\bar{\nu})d\bar{\nu} = 4.319\times 10^{-9}\frac{\mathrm{mol}\cdot\mathrm{cm}^2}{1}\int \varepsilon(\bar{\nu})d\bar{\nu} \tag{87}$$

where:

- ε_0: The vacuum permittivity
- m_e: The electron mass
- c: The speed of light

- e: The elementary charge
- N_A: Avocadro's number
- $\varepsilon(\bar{\nu})$: The molar extinction coefficient is given in units of $1(\text{mol}\cdot\text{cm})$, as a function of $\bar{\nu}(1/\text{cm})$.

Above all are given in SI units, the integral in Eq.(86) is determined by integrating over the respective band in an absorption spectrum plotted as $\varepsilon(\bar{\nu})$ as a function of $\bar{\nu}$. For crystals with symmetries lower than cubic it is necessary to measure polarized absorption spectra and take the appropriate sum to obtain the unpolarized $\varepsilon(\bar{\nu})$ for use in Eq.(86). For example, tetragonal, hexagonal, and trigonal crystal systems are typically uniaxial, i.e. having an extraordinary axis $\vec{c}$ that is different from the other axes $\vec{a}$. In this case, the unpolarized $\varepsilon(\bar{\nu})$ is obtained by separately measuring the σ-polarized ($\vec{E}\perp\vec{c}$) and π-polarized ($\vec{E}\|\vec{c}$) absorption spectra and adding them according to $\varepsilon(\bar{\nu}) = 2\varepsilon_\sigma(\bar{\nu}) + \varepsilon_\pi(\bar{\nu})$. Unless the material is amorphous or of cubic symmetry, it is therefore critically important to measure all applicable polarizations separately and to properly add them to obtain the unpolarized absorption spectrum. Not doing so can introduce substantial errors in the oscillator strengths.

The same with barycenter energies E_B, we have to choose to either minimize the absolute root-mean-square (RMS) deviation or the relative RMS deviation(better) when fitting the oscillator strengths f_i^{exp} and f_i^{calc} to get the $\Omega_{(\lambda)}$.

$$\text{RMS}_{abs} = \sqrt{\frac{1}{n-p}\sum_{i=1}^{n}\left(f_i^{\text{exp}} - f_i^{calc}\right)^2} \tag{88}$$

$$\text{RMS}_{rel} = \sqrt{\frac{1}{n-p}\sum_{i=1}^{n}\left(\frac{f_i^{\text{exp}} - f_i^{\text{calc}}}{f_i^{\text{exp}}}\right)^2} \tag{89}$$

between the calculated and experimental oscillator strengths, where n is the number of experimental oscillator strengths and p is the number of fit parameters ($p = 3$ in this case).

In most cases, only the RMS_{rel} gave stable and physically meaningful values of the $\Omega_{(\lambda)}$ parameters. [59][60]. In particular, they were able to successfully predict the oscillator strength of the ${}^3\text{H}_4 \rightarrow {}^3\text{P}_2$ transition, which is notoriously difficult to model when fitting with RMS_{abs}.

9 Tables

9.1 Calculated ED Transition Rates of Tm^{3+}

Unit: s^{-1}	E_1	E_2	E_3	E_4	E_5	E_6	E_7
E_0	125.489	176.997	778.622	1725.686	548.821	612.189	7073.749
E_1		3.319	66.541	258.728	362.103	790.612	2862.411
E_2			34.206	146.531	192.816	494.834	94.779
E_3				0.492	5.142	23.045	2125.977
E_4					0.014	45.243	488.517
E_5						12.272	686.956
E_6							95.084

Table 5: Calculated ED transition rates of Tm^{3+}

Unit: s^{-1}	E_1	E_2	E_3	E_4	E_5	E_6	E_7	E_8	E_9	E_{10}
E_0	88.128	105.007	107.078	1009.622	919.104	2812.804	2256.276	1090.406	982.137	958.440
E_1		13.728	40.066	45.114	378.152	71.357	334.112	918.920	94.355	936.523
E_2			0.690	49.125	28.889	41.091	162.988	87.113	753.563	213.861
E_3				1.414	46.481	47.601	93.442	75.276	215.709	16.464
E_4					0.549	8.842	3.447	94.313	16.968	16.674
E_5						0.026	0.019	0.465	2.252	0.269
E_6							0.409	3.067	0.095	12.331
E_7								0.729	0.483	4.364
E_8									0.006	0.159
E_9										0.049

Table 6: Calculated ED transition rates of Er^{3+}

Unit: s^{-1}	E_{11}	E_{12}	E_{13}	E_{14}	E_{15}
E_0	9297.317	2130.746	410.568	968.789	353.042
E_1	1243.935	5387.633	42.735	455.366	1489.401
E_2	64.672	449.589	287.008	2389.063	955.067
E_3	94.459	13.845	196.579	1060.980	248.191
E_4	236.199	508.558	30.527	14.341	160.793
E_5	16.563	36.127	0.404	69.866	202.936
E_6	17.833	77.317	126.166	64.614	53.876
E_7	13.996	99.441	0.018	35.043	38.789
E_8	1.877	12.768	1.137	38.512	39.604
E_9	1.325	7.972	0.002	8.943	9.394
E_{10}	1.163	0.559	4.346	0.646	109.062
E_{11}		0.087	0.264	0.114	3.435
E_{12}			0.000	0.016	0.879
E_{13}				0.001	0.997
E_{14}					0.675

Table 7: Calculated ED transition rates of Er^{3+}

Unit: s^{-1}	E_1	E_2	E_3	E_4	E_5	E_6	E_7
E_0	0	50.019	0	0	0	0	0
E_1		0	0	58.982	0	0	0
E_2			7.408	0	0	0	0
E_3				0	0	0	0
E_4					0.018	0	0
E_5						0	0
E_6							0

Table 8: Calculated MD transition rates of Tm^{3+}

Unit: s^{-1}	E_1	E_2	E_3	E_4	E_5	E_6	E_7	E_8	E_9	E_{10}
E_0	38.867	0	0	0	0	0	0	0	0	0
E_1		8.297	0	0	0	0	0	0	0	0
E_2			1.705	0	0	0	0	0	0	0
E_3				0	0	0	0	0	0	0
E_4					0	0	17.837	0	0	0
E_5						0	0	0	0	0
E_6							0	0	0	0
E_7								0.967	0	0
E_8									0.008	0
E_9										0

Table 9: Calculated MD transition rates of Er^{3+}

9.2 Calculated ED Transition Rates of Er^{3+}

9.3 Calculated MD Transition Rates of Tm^{3+}

9.4 Calculated MD Transition Rates of Er^{3+}

9.5 Calculated MPR Rates of Tm^{3+}

9.6 Calculated MPR Rates of Er^{3+}

9.7 Calculated Resonant ET Rates of Yb^{3+}

9.8 Calculated Up-conversion Rates of Yb^{3+}-Tm^{3+}

9.9 Calculated Cross-relaxation Rates of Tm^{3+}-Tm^{3+}

9.10 Calculated Up-conversion Rates of Yb^{3+}-Er^{3+}

9.11 Calculated Cross-relaxation Rates of Er^{3+}-Er^{3+}

9.12 Emory: ED Transition Rates of Er^{3+}+Tm^{3+}

9.13 Emory: ED Transition Rates of Er^{3+}

9.14 Weber: ED Transition Rates of Er^{3+}

9.15 Weber: MD Transition Rates of Er^{3+} ($n = 2.02$)

9.16 Weber: MD Transition Rates of Er^{3+} ($n = 1.5$)

Unit: s^{-1}	E_{11}	E_{12}	E_{13}	E_{14}	E_{15}
E_0	0	0	0	0	0
E_1	0	0	0	0	0
E_2	0	0	0	0	0
E_3	0	0	0	0	0
E_4	0	0	0	0	0
E_5	0	0	0	0	0
E_6	0	0	0	0	0
E_7	0	0	0	0	0
E_8	0	0	0	0	0
E_9	0	0	0	0	0
E_{10}	0	0	0	1.705	0
E_{11}		0.110	0	0	0
E_{12}			0	0	0
E_{13}				0	0
E_{14}					0

Table 10: Calculated MD transition rates of Er^{3+}

Unit: s^{-1}	E_1	E_2	E_3	E_4	E_5	E_6	E_7
E_0	0	0	0	0	0	0	0
E_1		149977.840	0	0	0	0	0
E_2			0	0	0	0	0
E_3				1768677.821	230669.870	0	0
E_4					156605871.044	0	0
E_5						0	0
E_6							0

Table 11: MPR rate of Tm^{3+}

Unit: s^{-1}	E_1	E_2	E_3	E_4	E_5	E_6	E_7	E_8	E_9
E_0	0	0	0	0	0	0	0	0	0
E_1		0	0	0	0	0	0	0	0
E_2			353536.790	0	0	0	0	0	0
E_3				78491.281	0	0	0	0	0
E_4					0	0	0	0	0
E_5						73532852.089	0	0	0
E_6							15062862.443	0	0
E_7								2323866.222	0
E_8									301337914.186
E_9									

Table 12: MPR rate of Er^{3+}.

Unit: s^{-1}	E_{10}	E_{11}	E_{12}	E_{13}	E_{14}	E_{15}
E_0	0	0	0	0	0	0
E_1	0	0	0	0	0	0
E_2	0	0	0	0	0	0
E_3	0	0	0	0	0	0
E_4	0	0	0	0	0	0
E_5	0	0	0	0	0	0
E_6	0	0	0	0	0	0
E_7	0	0	0	0	0	0
E_8	557235.27	0	0	0	0	0
E_9	2220499.729	0	0	0	0	0
E_{10}		1548415.691	57081.927	0	0	0
E_{11}			0	17509301.842	7532539.783	0
E_{12}				474960799.640	204329170.347	0
E_{13}					516581089.114	0
E_{14}						0

Table 13: MPR rate of Er^{3+}

Unit: cm^6/s	$S_1 \to S_0 \Rightarrow S_0 \to S_1$	$S_1 \to S_0 \Rightarrow S_0 \to S_1$
Values	7.03×10^{-39} (s=0.001)	9.84×10^{-40} (s=0.00014)

Table 14: Resonant energy transfer rate of Yb^{3+}

Unit: cm^6/s	$S_1 \to S_0 \Rightarrow E_2 \to E_0$	$S_1 \to S_0 \Rightarrow E_4 \to E_1$	$S_1 \to S_0 \Rightarrow E_6 \to E_3$	$S_1 \to S_0 \Rightarrow E_7 \to E_6$
Values	8.82×10^{-42}	2.82×10^{-41}	2.51×10^{-42}	2.55×10^{-43}

Table 15: Up-conversion of Yb^{3+}-Tm^{3+}

Unit: cm^6/s	$E_3 \to E_1 \Rightarrow E_1 \to E_0$	$E_6 \to E_2 \Rightarrow E_3 \to E_0$	$E_7 \to E_5 \Rightarrow E_3 \to E_0$
Values	2.05×10^{-41}	7.30×10^{-41}	1.29×10^{-40}

Table 16: Cross-relaxation of Tm^{3+}-Tm^{3+}

Unit: cm^6/s	$S_1 \to S_0 \Rightarrow E_2 \to E_0$	$S_1 \to S_0 \Rightarrow E_7 \to E_2$	$S_1 \to S_0 \Rightarrow E_{15} \to E_7$
Values	1.29×10^{-40}	1.74×10^{-40}	7.06×10^{-42}

Table 17: Up-conversion processes of $Yb^{3+} \to Er^{3+}$

Unit: cm^6/s	$E_3 \to E_1 \Rightarrow E_1 \to E_0$	$E_7 \to E_2 \Rightarrow E_2 \to E_0$	$E_4 \to E_2 \Rightarrow E_1 \to E_0$	$E_8 \to E_3 \Rightarrow E_2 \to E_0$
Values	2.52×10^{-41}	2.29×10^{-41}	1.05×10^{-41}	4.42×10^{-42}

Table 18: Cross-relaxation processes of Er^{3+}

Er^{3+}+Tm^{3+}	$^4F_{9/2} \to {}^4I_{15/2}$	$^4S_{3/2} \to {}^4I_{15/2}$	$^3F_4 \to {}^3H_6$
Emory (Unit: nm^{-3}/s)	0.029	0.001	2.353
Our calculation (Unit: nm^{-3}/s)	0.0282	0.00054	2.3429
Relative Error	2.76%	46.0%	0.430%

Table 19: ED-radiative emission (Emory: Er^{3+}+Tm^{3+})

Er^{3+}	$^4F_{9/2} \to {}^4I_{15/2}$	$^4S_{3/2} \to {}^4I_{15/2}$	$^4I_{13/2} \to {}^4I_{15/2}$
Emory (Unit: nm^{-3}/s)	0.005	0.004	0.858
Our calculation (Unit: nm^{-3}/s)	0.0051	0.0037	0.8590
Relative Error	2.00%	7.50%	0.117%

Table 20: ED-radiative emission (Emory: Er^{3+} alone)

Er^{3+}	$^4I_{13/2} \rightarrow {}^4I_{15/2}$	$^4I_{11/2} \rightarrow {}^4I_{15/2}$	$^4I_{11/2} \rightarrow {}^4I_{13/2}$
Weber (Unit: s^{-1})	54 (validation)	70	7.7
Our calculation (Unit: s^{-1})	n=2.02	71.77	8.45
Relative Error	N/A	2.53%	9.74%

Table 21: ED-radiative emission

Er^{3+}	$^4I_{13/2} \rightarrow {}^4I_{15/2}$	$^4I_{11/2} \rightarrow {}^4I_{13/2}$	$^4I_{9/2} \rightarrow {}^4I_{11/2}$
Weber (Unit: s^{-1})	37.6	8.4	1.2
Our calculation (Unit: s^{-1})	78.700	18.167	2.626
Relative Error	109.31%	116.27%	118.83%

Table 22: MD-radiative emission ($n = 2.02$, intermediate coupling wavefunction)

Er^{3+}	$^4I_{13/2} \rightarrow {}^4I_{15/2}$	$^4I_{11/2} \rightarrow {}^4I_{13/2}$	$^4I_{9/2} \rightarrow {}^4I_{11/2}$
Weber (Unit: s^{-1})	37.6	8.4	1.2
Our calculation (Unit: s^{-1})	38.87	8.30	1.71
Relative Error	3.38%	1.19%	42.5%

Table 23: MD-radiative emission ($n = 1.5$, pure wavefunction)